Multiparameter full waveform inversion of multicomponent ocean-bottom-cable data from the Valhall field. Part 2: imaging compressive-wave and shear-wave velocities

Vincent Prieux,[1] Romain Brossier,[2] Stéphane Operto[1] and Jean Virieux[2]

[1]*Géoazur, Université Nice-Sophia Antipolis, CNRS, IRD, Observatoire de la Côte d'Azur, Valbonne, CGG Massy, France. E-mail: vincent.prieux@cgg.com*
[2]*ISTerre, Université Joseph Fourier Grenoble 1, CNRS, Grenoble, France*

SUMMARY

Multiparameter elastic full waveform inversion (FWI) is a promising technology that allows inferences to be made on rock and fluid properties, which thus narrows the gap between seismic imaging and reservoir characterization. Here, we assess the feasibility of 2-D vertical transverse isotropic visco-elastic FWI of wide-aperture multicomponent ocean-bottom-cable data from the Valhall oil field. A key issue is to design a suitable hierarchical data-driven and model-driven FWI workflow, the aim of which is to reduce the nonlinearity of the FWI. This nonlinearity partly arises because the shear (*S*) wavespeed can have a limited influence on seismic data in marine environments. In a preliminary stage, visco-acoustic FWI of the hydrophone component is performed to build a compressional (*P*)-wave velocity model, a density model and a quality-factor model, which provide the necessary background models for the subsequent elastic inversion. During the elastic FWI, the *P* and *S* wavespeeds are jointly updated in two steps. First, the hydrophone data are inverted to mainly update the long-to-intermediate wavelengths of the *S* wavespeeds from the amplitude-versus-offset variations of the *P–P* reflections. This *S*-wave velocity model is used as an improved starting model for the subsequent inversion of the better-resolving data recorded by the geophones. During these two steps, the *P*-wave velocity model is marginally updated, which supports the relevance of the visco-acoustic FWI results. Through seismic modelling, we show that the resulting visco-elastic model allows several *P*-to-*S* converted phases recorded on the horizontal-geophone component to be matched. Several elastic quantities, such as the Poisson ratio, and the ratio and product between the *P* and *S* wavespeeds, are inferred from the *P*-wave and *S*-wave velocity models. These attributes provide hints for the interpretation of an accumulation of gas below lithological barriers.

Key words: Inverse theory; Elasticity and anelasticity; Controlled source seismology; Computational seismology; Wave propagation.

INTRODUCTION

Subsurface lithology and reservoir characterization require quantitative estimations of the physical rock properties. The joint knowledge of the compressional (*P*)-wave and shear (*S*)-wave velocities is of primary interest for better fluid characterization (Gregory 1976) as a potential indicator of hydrocarbon reservoirs (Tatham & Stoffa 1976), or to estimate porosity and grain size through empirical relationships between porosity and the *P* or *S* wavespeeds (Domenico 1984). Shear wave velocity models can also be used for the processing of multicomponent seismic data, as for wavefield decomposition or static corrections (Muyzert 2000). Full waveform inversion (FWI, Virieux & Operto 2009) is today mostly used to derive

P-wave velocity background models in acoustic approximations for reverse-time migration (Sirgue *et al.* 2010). However, multiparameter FWI based on the visco-elastic wave equation provides the necessary framework to evolve beyond the velocity model building task, and to derive more realistic multiparameter subsurface models, as promoted by Tarantola (1986), Shi *et al.* (2007), Sears *et al.* (2008), Brossier (2011) and others. Applications of elastic FWI to real data remain challenging because of the computational cost of the elastic modelling, which is between one and two orders of magnitude more expensive in two dimensions than its acoustic counterpart (Brossier 2011), and the strong nonlinearity of the elastic multiparameter inversion. In marine environments, the nonlinearity of the elastic FWI of streamer or multicomponent ocean-bottom seismic data can

GJI Seismology

result from the limited influence of the *S* wavespeed on the data, as a *P*-to-*S* conversion at the seabed or at deeper interfaces must occur to record *S* waves (Sears *et al.* 2008; Brossier *et al.* 2010b). On land, it is still an open question whether high-amplitude surface waves carry useful and manageable information for FWI (Brossier *et al.* 2009a; Baumstein *et al.* 2011).

Pioneering applications of elastic FWI to marine and land data sets have been presented previously, where the *P* and/or *S* wavespeeds (V_P, V_S), the elastic impedances (I_P, I_S) and the Poisson ratio (ν) have been reconstructed from short-spread reflection data (with less than 5 km offset) (Crase *et al.* 1990, 1992; Sun & McMechan 1992; Igel *et al.* 1996; Djikpéssé & Tarantola 1999a). More recently, the application of FWI to long-spread streamer data was also presented by Freudenreich *et al.* (2001) and Shipp & Singh (2002), although only the *P* wavespeed was updated during the inversion in this latter study.

The recording of multicomponent wide-aperture data is a key for the success of multiparameter elastic FWI, in addition to the recording of low frequencies (Manukyan *et al.* 2012). It is well acknowledged that short-spread streamer acquisitions do not allow for the reconstruction of the intermediate wavelengths of the subsurface, because of the insufficient wide-aperture illumination (i.e. large scattering angles) (Jannane *et al.* 1989; Neves & Singh 1996). This justifies the scale separation that underlies the two main tasks of the workflow of conventional seismic reflection processing: velocity macro-model building by traveltime tomography or migration-based velocity analysis, and reflectivity imaging by migration. Wide-aperture geometries provide a suitable framework to build the long and intermediate wavelengths of the subsurface from long-offset data, and hence they continuously sample the wavenumber spectrum of this subsurface (Sirgue & Pratt 2004). Secondly, wide-aperture multicomponent recordings are necessary to provide all of the scattering modes (the *P–P, P–S, S–P* and *S–S* diffractions) over a sufficiently broad range of scattering angles, which should help in the reconstruction of the *S*-wave velocity model. This is even more critical in marine environments, where the waves should undergo at least one *P*-to-*S* conversion to allow for *S*-wave recording by sea-bottom acquisitions. Furthermore, the amount of *P*-to-*S* conversion can be quite limited in the case of a soft seabed environment, and in particular with the recording times used in classical surveys. Another key issue related to *S*-wave velocity imaging is the building of a sufficiently accurate starting model for FWI. The smaller wavelengths of the shear wavefields make the reconstruction of the *S*-wave velocity subject to cycle skipping artefacts, and this might prevent the continuous sampling of the wavenumber spectrum of the *S*-wave velocity model. A second difficulty is related to the picking of reliable *P*-to-*S* converted phases for reflection-traveltime tomography: the construction of an initial *S*-wave model is therefore more difficult than the construction of an initial *P*-wave model.

Mitigating nonlinearities is challenging, especially when elastic seismic data are considered. The strategy for feeding the optimization procedure by the seismic data is of primary importance, and this can lead to the success or failure of the inversion procedure (Brossier *et al.* 2009b). The selection of the parameters is also of importance, and they might have different footprints in the recorded data. Many hierarchical FWI strategies can be viewed to reduce the nonlinearity of the inversion when multicomponent data are inverted to reconstruct multiple classes of parameters (e.g. Tarantola 1986). A data-driven level of hierarchy can be designed by proceeding from the inversion of low frequencies to higher ones, such that in the framework of multi-scale imaging, the large wavelengths of the

subsurface are reconstructed before the smaller ones (e.g. Bunks *et al.* 1995; Sirgue & Pratt 2004). Additional data preconditioning can be viewed to inject progressively more resolution or more complex information into the inversion, by proceeding from early arrivals to later arrivals (Brossier *et al.* 2009b), or by proceeding from short offsets to longer offsets in the framework of the layer-stripping strategies (Shipp & Singh 2002; Wang & Rao 2009). In the framework of multicomponent data, the hierarchy with which the data components are injected into the inversion is also a key feature, as the sensitivity of the data to one model parameter can depend on the data component (e.g. hydrophone versus geophone) (Sears *et al.* 2008, 2010). When multiparameter inversion is performed, additional levels of hierarchy in the model space can also be considered during FWI. First, the imaging of the parameters that have a dominant influence on the data can be chosen, before the imaging of the secondary parameters (Tarantola 1986). Secondly, the model parameters that have influence on the wide-aperture components of the data can be reconstructed before those that have influence on the short-aperture components of the data. According to the relationship between the aperture (or the scattering) angles and the wavenumber spanned in the model (Miller *et al.* 1987; Pratt & Worthington 1990; Jin *et al.* 1992; Sirgue & Pratt 2004), this strategy implies that the long wavelengths of the former category of parameters is reconstructed before the short wavelengths of the later category of parameters, hence honouring the multi-scale approach of FWI. A feasibility analysis of elastic FWI of multicomponent ocean-bottom seismic data was presented by Sears *et al.* (2008). They proposed a hierarchical approach, where the intermediate wavelengths of the *S* wavespeeds are first updated from the amplitude-versus-offset (AVO) variations of the *P–P* reflections on the hydrophone component. Although the influence of the shear-impedance contrasts on the *P–P* reflection is one order of magnitude smaller than that of the *P*-wave impedance (Igel & Schoenberg 1995), the information carried by the *P–P* scattering mode to reconstruct the intermediate wavelengths of the *S*-wave velocity model is quite important in marine environments. Indeed, the elastic inversion of the wide-aperture *P–P* reflection wavefield can be seen as a tool to build a reliable *S*-wave starting velocity model for the waveform inversion of the more resolving *P*-to-*S* converted phases recorded on the geophone components. In this study, we will reproduce this hierarchical approach that was presented in Sears *et al.* (2008).

We demonstrate an application of 2-D, multiparameter elastic FWI of multicomponent wide-aperture data recorded by ocean-bottom cables (OBCs) in the Valhall field. The reconstruction of the first *P*-wave velocity model, density model and attenuation model from the hydrophone component in the visco-acoustic approximation was presented in a companion report that we refer to as 'Paper I' in the following (Prieux *et al.* 2013). In the first part, we review the main features of the elastic FWI method that we use. Then, we review several aspects of multiparameter FWI of multicomponent data. In particular, the three key issues that are addressed are the choice of the subsurface parametrization for elastic FWI, the hierarchy with which the different classes of parameters are updated, and the hierarchy with which the different data components are inverted. After a qualitative interpretation of the data and the description of the set-up of the FWI, we present the FWI *P*-wave and *S*-wave velocity models, and we validate their relevance against sonic logs, seismic modelling and source wavelet estimation. Finally, from the FWI velocity models, we build some elastic properties, such as the Poisson ratio, and the product and ratio between the *P* and *S* wavespeeds, that are amenable to geological interpretations.

VISCO-ELASTIC FULL WAVEFORM INVERSION OF MULTICOMPONENT DATA

We seek to reconstruct the vertical *P* wavespeed and the *S* wavespeed by visco-elastic vertical transverse isotropic (VTI) FWI of the hydrophone and geophone data. Large-scale models of the anisotropic parameters δ and ϵ are kept fixed, and were inferred by 3-D anisotropic reflection traveltime tomography (courtesy of British Petroleum). FWI is performed in the frequency domain by local optimization, where the gradient of the misfit function is computed with the adjoint-state method (Plessix 2006; Chavent 2009). More specifically, a frequency-domain, velocity-stress, finite-element, discontinuous Galerkin method based on piecewise constant (P0), linear (P1) and quadratic (P2) interpolation functions (Brossier *et al.* 2010a; Brossier 2011) is used for the computing of the incident and adjoint wavefields. At the same time, a forward-modelling operator based on the second-order wave equation for particle velocities and the P0 interpolation function is used to build the diffraction kernel of the FWI from self-adjoint operators (see Paper I and Brossier (2011)).

The misfit function $\mathcal{C}(\mathbf{m})$ is given by:

$$
\mathcal{C}(\mathbf{m}) = \frac{1}{2} \sum_{j=1}^{N_c} \Delta \mathbf{d}_j^{\dagger} \mathbf{W}_{d_j} \Delta \mathbf{d}_j
$$
$$
+ \frac{1}{2} \sum_{i=1}^{N_p} \lambda_i \left(\mathbf{m}_i - \mathbf{m}_{\text{prior}_i} \right)^{\dagger} \mathbf{W}_{m_i} \left(\mathbf{m}_i - \mathbf{m}_{\text{prior}_i} \right), \quad (1)
$$

where $\Delta \mathbf{d} = (\Delta \mathbf{d}_1, \ldots, \Delta \mathbf{d}_{N_c})$ and N_c denote the multicomponent, data-residual vector and the number of data components involved in the inversion, respectively. In this study, N_c is equal to 1 or 2, depending whether the hydrophone or the two geophone components are considered during the inversion. Each component *j* of the data residual vector is weighted by the weighting matrix $\mathbf{W}_{d_j}$. This matrix can weight the data residuals according to the standard error and/or according to the source–receiver offsets (Ravaut *et al.* 2004; Operto *et al.* 2006). The multiparameter subsurface model is denoted by $\mathbf{m} = (\mathbf{m}_1, \ldots, \mathbf{m}_{N_p})$, where N_p denotes the number of parameter classes. In this study, the two classes of parameter are the vertical *P* wavespeed and the *S* wavespeed, which are jointly updated here. A Tikhonov regularization is applied to each parameter class *i* through a weighting operator $\mathbf{W}_{m_i}$, which forces the difference between the model $\mathbf{m}_i$ and the prior model $\mathbf{m}_{\text{prior}_i}$ to be smooth. The scalars λ_i control the weight of the data-space misfit function $\frac{1}{2} \sum_{j=1}^{N_c} \Delta \mathbf{d}_j^{\dagger} \mathbf{W}_d \Delta \mathbf{d}_j$ relative to the model-space misfit functions $(\mathbf{m}_i - \mathbf{m}_{\text{prior}_i})^{\dagger} \mathbf{W}_{m_i} (\mathbf{m}_i - \mathbf{m}_{\text{prior}_i})$. Of note, the scalar λ_i can be adapted to each parameter class *i*, which helps to account for the variable sensitivity of the data to each parameter class, as shown in Paper I.

The solution for the perturbation model, which minimizes the misfit function at iteration *k*, is given by:

$$
\Delta \mathbf{m}^{(k)} =
$$
$$
\Re \left(\widehat{\mathbf{W}}_m^{-1} \mathbf{J}^{(k)t} \widehat{\mathbf{W}}_d \mathbf{J}^{(k)t} + \widehat{\mathbf{W}}_m^{-1} \left(\frac{\partial \mathbf{J}^{(k)t}}{\partial \mathbf{m}^T} \right) \left(\Delta \mathbf{d}^{(k)*} \ldots \Delta \mathbf{d}^{(k)*} \right) + \Lambda \right)^{-1}
$$
$$
\times \Re \left(\widehat{\mathbf{W}}_m^{-1} \mathbf{J}^{(k)t} \widehat{\mathbf{W}}_d \Delta \mathbf{d}^{(k)*} + \Lambda \left(\mathbf{m}^{(k)} - \mathbf{m}_{\text{prior}} \right) \right), \quad (2)
$$

where Λ is a block diagonal damping matrix that can be expressed as:

$$
\Lambda = \begin{pmatrix} \lambda_1 \mathbf{I}_M & \ldots & \mathbf{0} \\ \ldots & \ldots & \ldots \\ \mathbf{0} & \ldots & \lambda_{N_p} \mathbf{I}_M, \end{pmatrix} \quad (3)
$$

where $\mathbf{I}_M$ is the identity matrix of dimension *M*, the number of parameter unknowns per class of parameter. In eq. (2), $\Re$ is the real part of a complex number. The matrices $\widehat{\mathbf{W}}_d$ and $\widehat{\mathbf{W}}_m$ are $N_c \times N_c$ and $N_p \times N_p$ block diagonal matrices, where each block is formed by the $\mathbf{W}_{d_j}$ and $\mathbf{W}_{m_i}$ matrices, respectively. The first term in eq. (2) is the inverse of the full Hessian, while the second term in eq. (2) is the gradient of the misfit function. In eq. (2), the matrix $\mathbf{J}$ is the sensitivity matrix, the coefficients of which are the values of the partial derivative of the wavefields with respect to the model parameters at the receiver positions. These partial derivative wavefields are the solution of the wave equation:

$$
\mathbf{B}(\omega, \mathbf{m}(\mathbf{x})) \frac{\partial \mathbf{v}(\omega, \mathbf{x})}{\partial m_l} = -\frac{\partial \mathbf{B}(\omega, \mathbf{m}(\mathbf{x}))}{\partial m_l} \mathbf{v}(\omega, \mathbf{x}), \quad (4)
$$

where $\mathbf{B}(\omega, \mathbf{m}(\mathbf{x}))$ is the forward-problem operator, and $\mathbf{v}$ is the incident particle velocity wavefield. The right-hand side of eq. (4) is the secondary virtual source of the partial derivative wavefield, the spatial support and temporal support of which are centred on the position of the diffractor m_l (the index *l* runs over all of the parameters) and on the arrival time of the incident wavefield at the diffractor m_l, respectively (Pratt *et al.* 1998). The scattering or diffraction pattern of this virtual source is given by $\partial \mathbf{B}(\omega, \mathbf{m}(\mathbf{x}))/\partial m_l$, which gives some insight into the sensitivity of the data to the parameter m_l as a function of the scattering (or aperture) angle.

We use the quasi-Newton limited-memory Broyden-Flechter-Goldfarb-Shanno (L-BFGS) optimization algorithm for solving eq. (2) (Nocedal 1980; Nocedal & Wright 1999). The L-BFGS algorithm computes recursively an approximation of the product of the inverse of the Hessian with the gradient, from a few gradients and a few solution vectors from the previous iterations. As an initial guess for this iterative search, we use a diagonal approximation of the approximate Hessian (the linear term) damped by the Λ matrix,

$$
H_0 = \left(\widehat{\mathbf{W}}_m^{-1} \text{diag} \left\{ \mathbf{J}^{(k)\dagger} \widehat{\mathbf{W}}_d \mathbf{J}^{(k)} \right\} + \Lambda \right)^{-1}. \quad (5)
$$

There are various expressions of eq. (2) (Greenhalgh *et al.* 2006) that can be selected for implementation convenience. Our implementation allows the pre-conditioner of the L-BFGS algorithm (eq. 5) to be diagonal, and hence easy to invert, because matrix Λ is diagonal, unlike $\widehat{\mathbf{W}}_m$. The smoothing operators $\mathbf{W}_{m_i}^{-1}$ are Laplace functions that are given by:

$$
\mathbf{W}_{m_i}^{-1}(z, x, z', x') = \sigma_i^2(z, x) \exp\left(\frac{-|x - x'|}{\tau_x} \right) \exp\left(\frac{-|z - z'|}{\tau_z} \right), \quad (6)
$$

where quantities τ_x and τ_z denote the horizontal and vertical correlation lengths, defined as a fraction of the local wavelength. The coefficient σ_i represents the standard error and can be scaled to the physical unit or to the order of magnitude of the parameter class *i*. A Laplace function is used for $\mathbf{W}_{m_i}^{-1}$, because its inverse in the expression of the misfit function can be computed analytically (Tarantola 2005, p. 97–99).

WHICH PARAMETRIZATION FOR ELASTIC FULL WAVEFORM INVERSION?

The choice of the subsurface parametrization should be driven by at least three criteria: (i) The sensitivity of the data to the parameter with respect to the scattering angle (which is referred to as the diffraction pattern of the parameter) should be as broad as possible, to guarantee a broadband reconstruction of the selected parameter. This sensitivity is given by the directivity of the virtual source in eq. (4). (ii) On the other hand, the trade-off between the parameter classes should be reduced as much as possible, which requires that the diffraction pattern of each parameter class does not significantly overlap as a function of the scattering angle. A suitable trade-off between these two criteria should be clearly found, as they cannot be simultaneously fulfilled. Note that the linear term of the Hessian is expected to partially correct the gradients of the misfit function with respect to different parameter classes from trade-off effects, eq. (2). However, the individual information coming from data recorded with different scattering angles are mixed in the Hessian and in the gradients after summation over the source–receiver pairs. This means that the information on the variable sensitivity of the data to different parameter classes as a function of the scattering angles is lost in eq. (2), which might prevent efficient correction of trade-off effects. Damping regularization in the Hessian is an additional feature to overcome the ill-conditioning of the Hessian, although fine tuning should be found to avoid the correction for trade-off effects from being hampered. (iii) Finally, the sensitivity of the data to the parameter for a significant range of scattering angles must be sufficiently high, such that the information content of the data can be extracted from the noise during the inversion. In this study, the subsurface model is parametrized by the vertical P wavespeed, the S wavespeed, the density, the quality factors and the Thomsen parameters δ and ϵ. Only the first two parameter classes are updated by FWI. Other possibilities involve the P and S slownesses, the P-wave and S-wave impedances, the Poisson ratio or the elastic moduli (Forgues & Lambaré 1997). A hierarchical reconstruction of the vertical P wavespeed, the density and the attenuation was performed in the visco-acoustic approximation for computational savings and this is described in Paper I. It is worth remembering that the ability to build a reliable P-wave velocity model with the acoustic FWI of the elastic data recorded by the hydrophone component was validated against a realistic synthetic example that is representative of the Valhall target by Brossier *et al.* (2009c). This is consistent with the conclusions of Barnes & Charara (2009), who showed the applicability of acoustic FWI in soft seabed environments. In Paper I, we followed a hierarchical approach where a model of the P wavespeed is first reconstructed before the joint update of this wavespeed, the density and the attenuation (Table 1). We favour a parametrization

for which the dominant parameter (namely, the P wavespeed) has an isotropic diffraction pattern, because the high-resolution model of the wavespeed obtained after the first inversion step is useful for the reconstruction of the density and attenuation during the second step. Of note, our conclusion differs from that of Debski & Tarantola (1995), who concluded that the (V_P, V_S, ρ) parametrization is not suitable for the reconstruction of the S wavespeed from this AVO information, because it leads to strongly correlated uncertainties. They advocated the use of other parametrizations such as (I_P, ν, ρ) or (I_P, I_S, ρ), for which the posterior probability density is maximally decoupled between the three parameters, with the largest error left on the density parameter.

The diffraction patterns of the P and S wavespeeds, which are computed in the asymptotic ray+Born approximation for the four scattering modes, P–P, P–SV, SV–P and SV–SV. These are shown in Fig. 1, with the consideration of an elastic isotropic medium parametrized by the P-wave and S-wave velocities and the density ρ (Forgues & Lambaré 1997). A P-wave velocity model perturbation generates only P–P diffraction with an isotropic diffraction pattern (Fig. 1a). Therefore, a broad-band reconstruction of this parameter is expected. An S-wave velocity-model perturbation generates P–P diffraction at intermediate scattering angles with smaller amplitudes than that generated by a P-wave velocity-model perturbation. Therefore, a low-pass filtered version of the S-wave velocity model is expected to be reconstructed from the hydrophone component, which is consistent with the results of Sears *et al.* (2008, 2010). The sensitivity of the hydrophone data to the S-wave velocity parameter (Aki & Richards 1980) is also shown by the different behaviours of the acoustic and elastic P–P reflection coefficients versus the angle beyond the critical incidence (Fig. 2) (Červený *et al.* 1977). The diffraction patterns of the S-wave velocity parameters for the last three scattering modes (P–SV, SV–P and SV–SV) are shown in Figs 1(b)–(d). The union of these three diffraction patterns covers the full range of scattering angles, with higher sensitivity of the SV–SV mode. Therefore, broad-band reconstruction of the S-wave
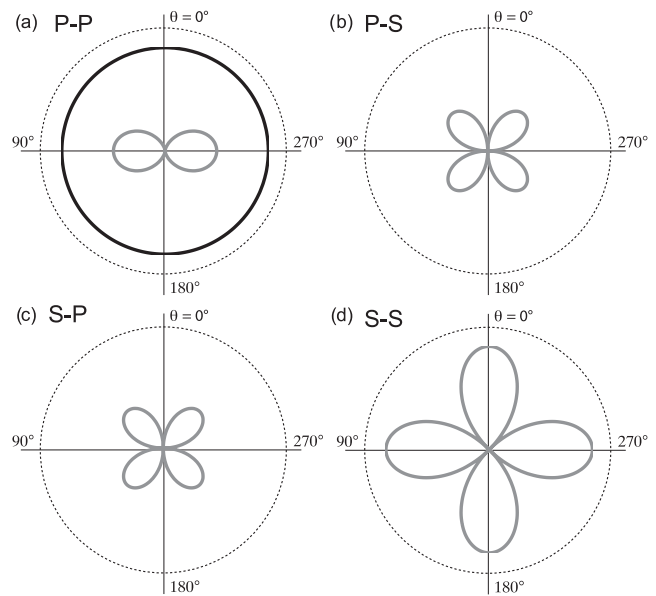
Table 1. The FWI experiments. The preliminary step of visco-acoustic FWI was described in Paper I. For application G, the geophone data are directly inverted to update the P and S wavespeeds. In applications H and HG, the hydrophone data are first inverted, before the inversion of the geophone data (see text for details).

Application	Step	Inverted data	Updated parameter	Approximation
	1	Hydrophone	V_{P0}	VTI visco-acoustic
	2		V_{P0}, ρ, Q_P	
G	3	Geophone		
H	3	Hydrophone	V_{P0}, V_S	VTI visco-elastic
HG	4	Geophone		

Figure 1. Radiation patterns of the P-wave (black) and the S-wave (gray) velocities for the P–P (a), P–SV (b), SV–P (c) and SV–SV (d) scattering modes computed in the ray+Born approximation (Forgues & Lambaré 1997). The diffraction patterns are plotted as polar coordinates as a function of the scattering (or aperture) angle. Note that a P-wave velocity perturbation generates only P–P diffraction with an isotropic diffraction pattern (a).
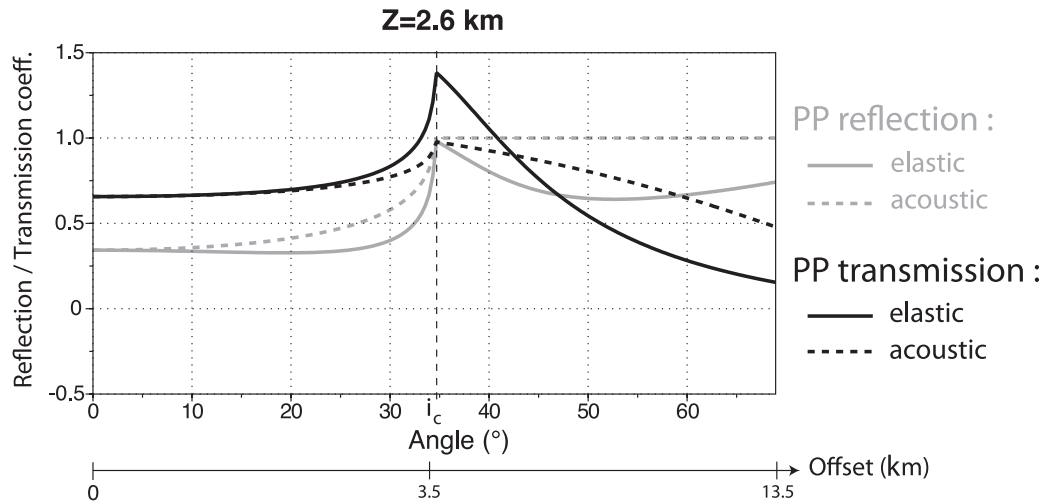
Figure 2. *P–P* reflection (gray) and transmission (black) amplitude displacement coefficients, with respect to the angle (and offset) at a liquid–liquid (dashed curves) and solid–solid (solid curve) interface (Červený *et al.* 1977) . The interface is at 2.6 km in depth at the reservoir level. The *P*-wave velocities in the upper and lower medium are 1700 m s^{-1} and 3000 m s^{-1}, the *S*-wave velocities are 650 and 1350 m s^{-1}, and the densities are 2020 and 2340 kg m^{-3}, respectively. These values are representative of the Valhall field. Note the differences between the acoustic and elastic AVO curves beyond the critical distance of 3.5 km.

velocity parameter is also expected if the four scattering modes can be exploited during FWI. The trade-off between the *P*-wave and *S*-wave velocity parameters is expected to be limited, because the diffraction patterns of the two classes of parameters overlap only for the *P–P* mode at intermediate scattering angles. We assume that this parametrization analysis, which is applied in the elastic isotropic approximation, will apply equally well to a visco-elastic VTI media. However, a detailed parametrization analysis of visco-elastic VTI FWI is left to future studies.

APPLICATION OF ELASTIC FULL WAVEFORM INVERSION TO VALHALL OBC DATA

Data and full waveform inversion set-up

The recording system consists of 220 multicomponent receivers on the sea bottom at 70 m in depth, and 320 explosive shots at 6 m below the sea surface. Two cables from the 3-D OBC survey (21 and 29) are included in this study (see Paper I, fig. 14). Cable 21 is located near the end of the gas cloud imaged in Sirgue *et al.* (2010) (between 1.5 and 2.5 km depth), while cable 29 is located off the gas cloud. Valhall is an old Triassic grabben which entered into compression during the later Cretaceous (Munns 1985), leading to the formation of an anticlinal which delineates the cap rock of the reservoir (at 2.5 km depth). The maximum source–receiver offset was 13 km.

Two forward problems are carried out per numerical source to build the gradient. We can use the spatial reciprocity of the Green's functions to use the physical sources as virtual receivers, and reciprocally. During the visco-elastic inversion of the hydrophone component, it is more efficient to exploit the reciprocity as there are more physical sources than hydrophones. As there are two components per receiver in the elastic case, we can perform either two simulations per physical sources or two simulations per vertical and horizontal geophone (treated as vertical and horizontal forces) to build the gradient. Considering that there are 320 independent sources in the real case and 440 independent receivers, it is more

efficient not to use the reciprocity and to keep the physical sources as numerical sources.

The additional cost of the elastic modelling is also due to the very low *S* wavespeeds at the sea bottom, which are four-times lower than the lowest *P* wavespeed. For the same spatial domain, this leads to a number of cells in the elastic mesh that is about 16-times greater than in the acoustic case. The maximum number of cells reaches 4.7×10^6 at 6.7 Hz, which prompted us to adapt the mesh size to the frequency.

During FWI, we considered the following five groups of three overlapping frequencies when we inverted the hydrophone data: $f_1 = $ [3.5, 3.78, 4], $f_2 = $ [4, 4.3, 4.64], $f_3 = $ [4.64, 5, 5.25], $f_4 = $ [5.25, 5.6, 6], $f_5 = $ [6, 6.35, 6.7] Hz, while we considered only the last four frequency groups for the geophone data inversion, as the signal-to-noise ratio of the geophone data is considered to be too poor in the [3.5–4] Hz frequency range. The recorded data are transformed in the frequency domain, considering 4 s and 8 s of the signals for the hydrophone and geophone components, respectively.

The FWI geophone data pre-processing consisted in minimum-phase whitening, followed by Butterworth filtering with cut-off frequencies of 3 and 20 Hz, a mute before the first arrival, and 3-D-to-2-D amplitude correction implemented by multiplying the data by $\sqrt{t}$. The 3-D-to-2-D correction consists of phase and amplitude correction (Bleistein 1986; Yedlin *et al.* 2010). Ravaut *et al.* (2004) showed that for their application of FWI to a thrust belt, the phase dependency of the 3-D-to-2-D correction was not critical in the frequency range considered (1–13 Hz). Yedlin *et al.* (2010) showed that the error of the amplitude correction performed by temporal scaling (on which a phase correction was added) is negligible as long as there are no lateral variations in the cross direction. The data are affected by platform noise, which consists of scattered waves that are emitted by the platform. We did not apply any denoising (like a *f–k* filtering) as this might have removed some useful events that have similar slopes in the data. Omitting the noisy traces is even worst, as this would have muted the early events (more energetic) that are less affected by the noise.

No time damping was applied to the hydrophone and geophone data during the inversion, and hence the full information content of the hydrophone and geophone data were used all together. Time damping is not necessary as the V_P starting model inferred by

visco-acoustic FWI already explains the acoustic wavefield, and we are interested in extracting information from the *P*-to-*S* converted waves, which are late arrivals. Moreover, no gain with offset was applied to the data during the inversion ($\mathbf{W}_d = \mathbf{I}$ in eq. 1). The L-BFGS optimization performed less than 10 iterations per frequency group, although the maximum number of iterations was set to 25. Our stopping criteria forces the inversion to stop as soon as the maximum velocity perturbation is lower than 10^{-3} per cent of the velocity of the starting model at the position of maximum velocity. A source wavelet per shot gather was estimated at each iteration of the hydrophone and geophone data by solving a linear inverse problem (see eq. 17 in Pratt 1999).

The standard errors σ_i, which are used in the weighting matrices $\mathbf{W}_{m_i}$, in eq. (2), are set to 1, because we normalize the subsurface parameters by their mean values (see Paper I). The damping factors λ_i are defined according to the amplitude of the partial derivative of the wavefields with respect to the parameter classes, which can be assessed from the diagonal terms of the approximate Hessian, eq. (5); namely, the auto-correlation of the partial derivative wavefields. The maximum value of the approximate Hessian associated with the vertical *P* wavespeed is on average four-times higher than that associated with the *S* wavespeed for all of the tests, and therefore we use a damping value for the *S* wavespeed that is four-times smaller than that used for the vertical *P* wavespeed. We will show in the following that this tuning allows reasonable agreement to be achieved between the FWI models and the sonic logs. The damping values used for the vertical *P* and *S* wavespeeds are outlined in Table 2.

In this study, the vertical *P* wavespeed and the *S* wavespeed are reconstructed simultaneously (Table 1). The initial vertical *P*-wave velocity model of the elastic inversion is the final model of the multiparameter visco-acoustic FWI (Fig. 3a and d) presented in Paper I (their figs 16h and 17e), and the initial *S*-wave velocity model was built by anisotropic reflection traveltime tomography (Figs 3b and e). The background models of the density, attenuation and Thomsen parameters are kept fixed to their initial values, and are described in Paper I. We simultaneously update V_P and V_S because V_P was previously obtained by visco-acoustic FWI. Fixing V_P would potentially lead to erroneous update of V_S because of the trade-off between these two parameters (data residuals resulting from missing V_P heterogeneities are interpreted as the result of missing V_S heterogeneities). We investigated two main data-driven strategies for the joint update of the vertical *P* wavespeed and the *S* wavespeed (Table 1): in strategy 1, the hydrophone data are first inverted to update the intermediate wavelengths of the *S* wavespeed using the AVO variations of the *P*–*P* reflections (Sears *et al.* 2008, 2010) (referred to as application *H* in the following). In the second step, the FWI velocity models that are built during step 1 are used as the starting models to invert the geophone data and to update the short wavelengths of both the vertical *P* wavespeed and the *S* wavespeed (referred to as application *HG* in the following). In strategy 2, the geophone data are directly inverted, to jointly update the vertical *P* wavespeed and the *S* wavespeed (referred to as application *G* in the following).

Full waveform inversion results

The elastic FWI models obtained with applications *H*, *HG* and *G* are shown for lines 29 and 21 in Figs 4 and 5, respectively. The starting and the final FWI vertical *P*-wave velocity models (Figs 3a, 3d, 4a, 4c, 4e and 5a, 5c, 5e) do not show significant differences; these differences reach a maximum of $\pm 250 \, \mathrm{m \, s^{-1}}$. Limited update of the vertical *P* wavespeed is expected, as the former inversion of the hydrophone data in the visco-acoustic approximation still provided a reliable model (Paper I). The vertical oscillations in the

Table 2. The FWI set-up. The inversion dampings λ for each parameter class.

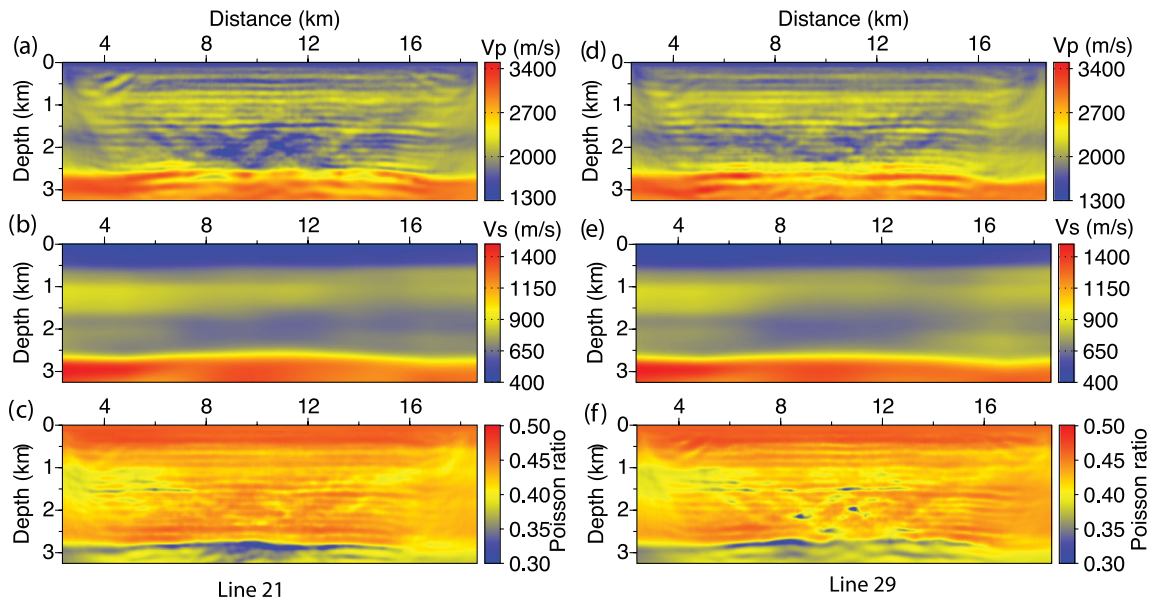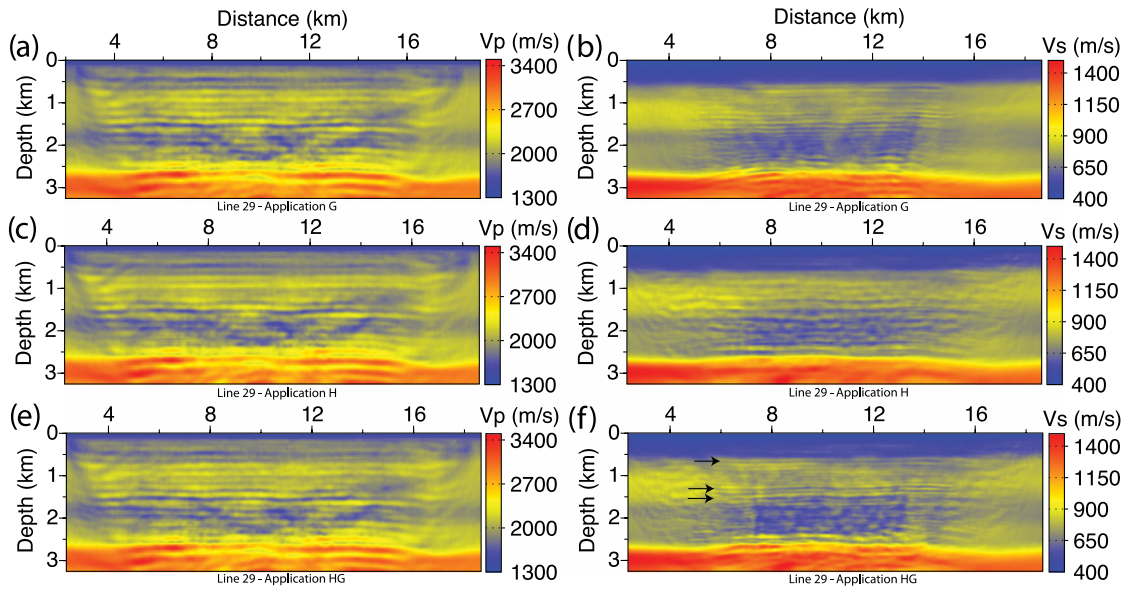| Parameter	λ
V_{P0} (m s^{-1})	4×10^{-8}
ρ (kg m^{-3})	4×10^{-8}
Q_P	4×10^{-10}
V_S (m s^{-1})	1×10^{-8}

Figure 3. Initial FWI models. (a, b, d, e) Starting *P*-wave (a, d) and *S*-wave (b, e) velocity models of elastic FWI for line 21 (a, b) and line 29 (d, e). (a, d) The *P*-wave velocity models were built by visco-acoustic FWI (Paper I). (b, e) The *S*-wave velocity models were built by anisotropic reflection traveltime tomography. (c, f) Poisson ratio models inferred from the *P*-wave and the *S*-wave velocity models shown in (a, b) and (d, e), respectively.

Figure 4. Final FWI models for line 29. The final *P*-wave velocity (a, c, e) and *S*-wave (b, d, f) velocity FWI models of applications *G* (a, b), *H* (c, d), and *HG* (e, f). Note that the reflectors are better delineated in the *S*-wave velocity FWI models of application *HG*, than in those of application *G*. Black arrows in the *S*-wave velocity model of application HG, depth of laterally continuous reflectors.
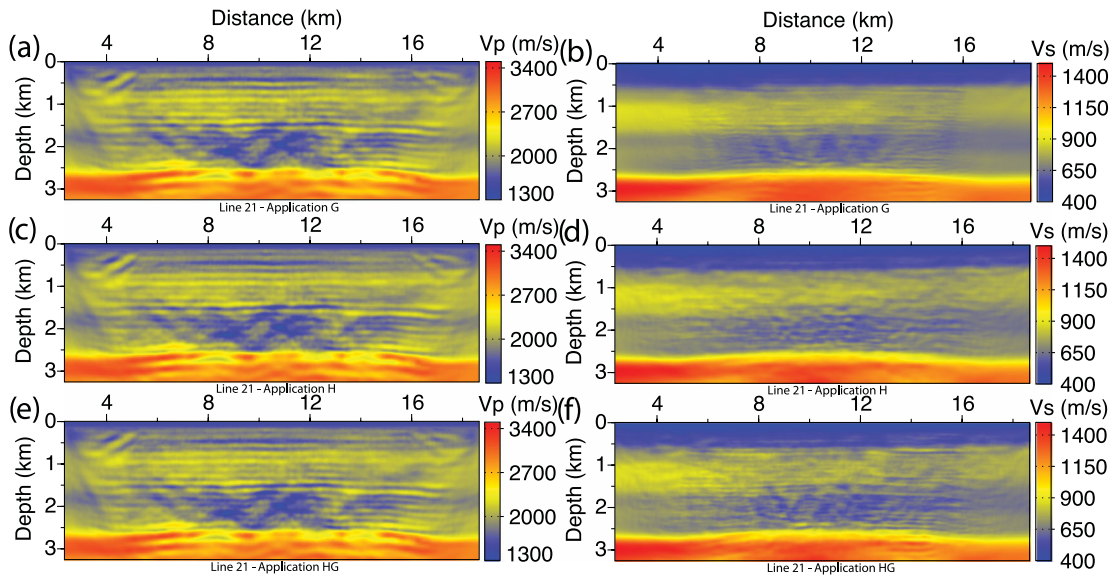

Figure 5. Final FWI models for line 21. The final *P*-wave velocity (a, c, e) and *S*-wave (b, d, f) velocity FWI models of applications *G* (a, b), *H* (c, d) and *HG* (e, f) for line 21. The results appear noisier than for line 29 (see Fig. 4).

V_P model are probably not real features. They might be related to layer-induced anisotropy, created to compensate for the kinematic inaccuracies of the anisotropic parameters at an intermediate offset shown in Prieux *et al.* (2011). Another possible reason is the narrow range of inverted frequencies in each group, which can lead to Gibbs effects in the imaging. The shaping approach of Lazaratos *et al.* (2011) would theoretically allow the spectrum of the gradient to be forced to mimic the spectrum of the true subsurface medium during the first iteration, to increase the lower frequency part of the spectrum and to minimize the necessary number of iterations to fully reach convergence. This shaping approach is only valuable for the reflection wavefield, while the Valhall acquisition is commonly considered as a wide-aperture data set (with up to 13 km maximum offset). As the imprint of the reflections is, however, significant in Valhall, it would nevertheless be worth investigating the

shaping approach of Lazaratos *et al.* (2011) although it remains beyond the scope of this study. The *S*-wave velocity model inferred from the hydrophone component during application *H* (Figs 4d and 5d) is smoother than that inferred from the geophone components during application *HG* (Figs 4f and 5f), which is consistent with the diffraction pattern analysis (Fig. 1) than states that an *S*-wave velocity perturbation generates a *P*–*P* diffraction at intermediate scattering angles. The final *S*-wave velocity models inferred from application *HG* (Figs 4f and 5f) shows thin continuous reflectors at 0.6, 1.25 and 1.5 km in depth (Fig. 4f, black arrows). These reflectors are sharper when the hierarchical inversion of the hydrophone and geophone data (application *HG*) is performed, compared to the inversion of the geophone components only (application *G*) (Figs 4b and 5b). This highlights the benefit of the data-driven hierarchical approach over the data component that is used in this study.

Model appraisal

Comparison with sonic logs

We first assessed the FWI *S*-wave velocity models against the sonic logs (Fig. 6). As already noted, the amplitudes of the *S*-wave velocity contrasts are weaker when only the geophone data are inverted (application *G*), relative to the hierarchical inversion of the hydrophone (application *H*) and geophone (application *HG*) data. The velocity contrasts are also weaker in the *S*-wave velocity model of line 21, relative to those of line 29. This might be related to the platform noise which has a greater effect on cable 21 as it is closer to the platform. An additional explanation is that the gas content in the medium, and consequently the attenuation of the *P* waves, is more important for line 21 than for line 29. Different 3-D effects between these two lines are another cause for differences in the results, which is consistent with line 21 being in the centre of the anticlinal and the gas cloud, while line 29 is more off-centre. The starting *S*-wave velocity model shows overestimated velocities in the gas relative to the sonic log. FWI fails to update the long wavelengths of the *S*-wave velocity model to match the trend of the sonic log in the gas; mainly short-wavelength perturbations are added by FWI, to match the small-scale structures of the sonic logs. This suggests that there is no information in the data to update the long-to-intermediate wavelengths of the gas layers of the *S*-wave velocity model. This lack of constraints on the long wavelengths of the *S*-wave velocity structure can be explained by the shorter propagated *S* wavelengths, relative to the *P* counterparts and by the narrow range of scattering angles over which the *P*-to-*S* converted waves are recorded. Moreover, at these depths, the target is poorly illuminated by the *P* diving waves and the *P* long-spread reflections, which would have contributed to the reconstruction of the long-to-intermediate wavelengths of the *S*-wave velocity model during application *H*. Nevertheless, we note that the elastic inversion tends to set velocities closer to the sonic log down to 700 m depth, in particular in the Figs 6(e) and (f), and that the inversion was clearly able to mark the contrasts from the top of the gas and of the reservoir, although with an under-estimated amplitude. The last frequency group generated consistent model perturbations, which reached up to 135 m s^{-1} for V_S (line 29). This suggested that we can continue inverting higher frequencies than 6.7 Hz, although this was above our computational resources. It would, however, probably lead to a local minimum as we have just shown that the long spatial wavelengths of the medium were missing.

Seismic modelling: anatomy of the data and the data fitting

An important assessment of the FWI results relies on the comparison between the recorded seismograms and the seismograms computed in the FWI models. Before showing this comparison, it is worth analysing the imprint of the elastic properties of the subsurface on the data. We focus here on the horizontal geophone, as the imprint of the *S*-wave velocity structure is only significant on this component. A shot gather recorded by the horizontal geophones is shown in Fig. 7(a), on which are superimposed the traveltime curves of the different types of converted waves computed by ray tracing in the FWI models of line 29 from application *HG*.

The arrivals labelled in the seismograms of Fig. 7(a) can be interpreted by examining a few snapshots of the wavefronts of the horizontal particle velocities, computed in the final FWI model of application *HG* with a VTI elastic finite-difference time-domain code (Fig. 8). The *P*–*P*, *P*–*S* and *S*–*S* converted waves that are

reflected from the four main interfaces at 0.6 km, 1.25, 1.5 and 2.6 km in depth can be clearly identified in these snapshots. Of note, in our nomenclature of the converted phases (*P*–*P*, *P*–*S*, *S*–*S*), we omit labelling of the *P*-wave propagation in the water layer. The traveltime curves of the *P* and *S* diving waves show a slope break at a cross-over distance of 3 km and 2 km, respectively, which corresponds to the distance beyond which the diving waves that propagate between 0.6 and 1.5 km in depth are recorded as first arrivals. We do not see any evidence of *S*–*S* waves in the seismograms recorded by the horizontal geophone (Fig. 7a), although *S*–*S* reflections from reflectors at 1.25 and 1.5 km in depth can be interpreted in the snapshots at the times of 3.6 and 5.2 s, with a non-negligible amplitude, and they are visible in the seismograms computed in the final FWI model of application *HG* (Fig. 7c). Ray tracing shows that the traveltime of the $SS_{2.6}$ reflection (from the reservoir level) is 7.8 s at zero offset (not shown in Fig. 7a), and hence it is not present in the recorded data, as the trace length is 8 s. We also show Scholte waves on all of the data components, with a wavespeed <350 m s^{-1}. These waves were not properly modelled, as we designed the mesh such that the lowest velocity that prevents numerical dispersion is 400 m s^{-1}.

The amplitudes of the *P*-to-*S* converted phases generally increase with depth, as the *S* wavespeed becomes closer to the *P* wavespeed (White & Stephen 1980); this arises from the rapid increase in the *S* wavespeed with depth (Hoven *et al.* 1991). The *P*-wavespeed over *S*-wavespeed ratio in the final FWI model of application *HG* is about 4 in the first 220 m in depth, then 3 down to 2.5 km in depth, and 2 below 2.5 km in depth. This explains the weak *P*-to-*S* conversion at the sea bottom, and why the strongest *P*-to-*S* conversion occurs at the reservoir level, as a ratio of 3 in the tertiary sediments is relatively high (Mueller *et al.* 1997).

To compare the recorded and modelled seismograms, we compute impulsional seismograms using a Dirac source wavelet within the [1–10] Hz frequency range, and we convolve these with the source wavelet estimated from the corresponding recorded data component, following the expression of Pratt (1999, eq. 17). We first compare the acoustic and elastic seismograms computed in the starting FWI models of line 29, to highlight the imprint of the *S* wavespeed on the elastic wavefields (Figs 7d and e). The main differences between the two sets of seismograms are related to the *S* diving waves and the *P*-to-*S* waves with a conversion at 2.6 km in depth. The main arrivals shown in both of the gathers are the *P*–*P* reflection from the top and the bottom of the gas layers. However, the $PS_{0.6}$, $PS_{1.25}$ and $PS_{1.5}$ converted waves are not visible in both sets of seismograms. The elastic seismograms computed in the final FWI models of application *H* show an enhanced $PS_{2.6}$ arrival and a weak $PS_{1.5}$ wave (Fig. 7b). All of the *P*-to-*S* waves that can be interpreted in the recorded gather are shown in the seismograms computed in the final FWI model of application *HG*, thus confirming that FWI successfully extracts this information (Fig. 7c). The *P*-to-*S* converted arrivals in the seismograms computed in the final FWI model of application *G* (Fig. 7f) have smaller amplitudes than those of the seismograms computed in the final FWI model of application *HG* (Fig. 7c), which supports the superiority of the hierarchical approach by successive inversions of the hydrophone and geophone components. A more detailed view of the waveform agreement for the horizontal component between the recorded and modelled data in the models of application *HG* for line 29 is provided in Fig. 9(a) by the direct comparison of the two sets of seismograms plotted with their true amplitudes and a gain with offset. The amplitudes of the computed data are underestimated for the *P*-to-*S* arrivals, although we note good phase agreement with the
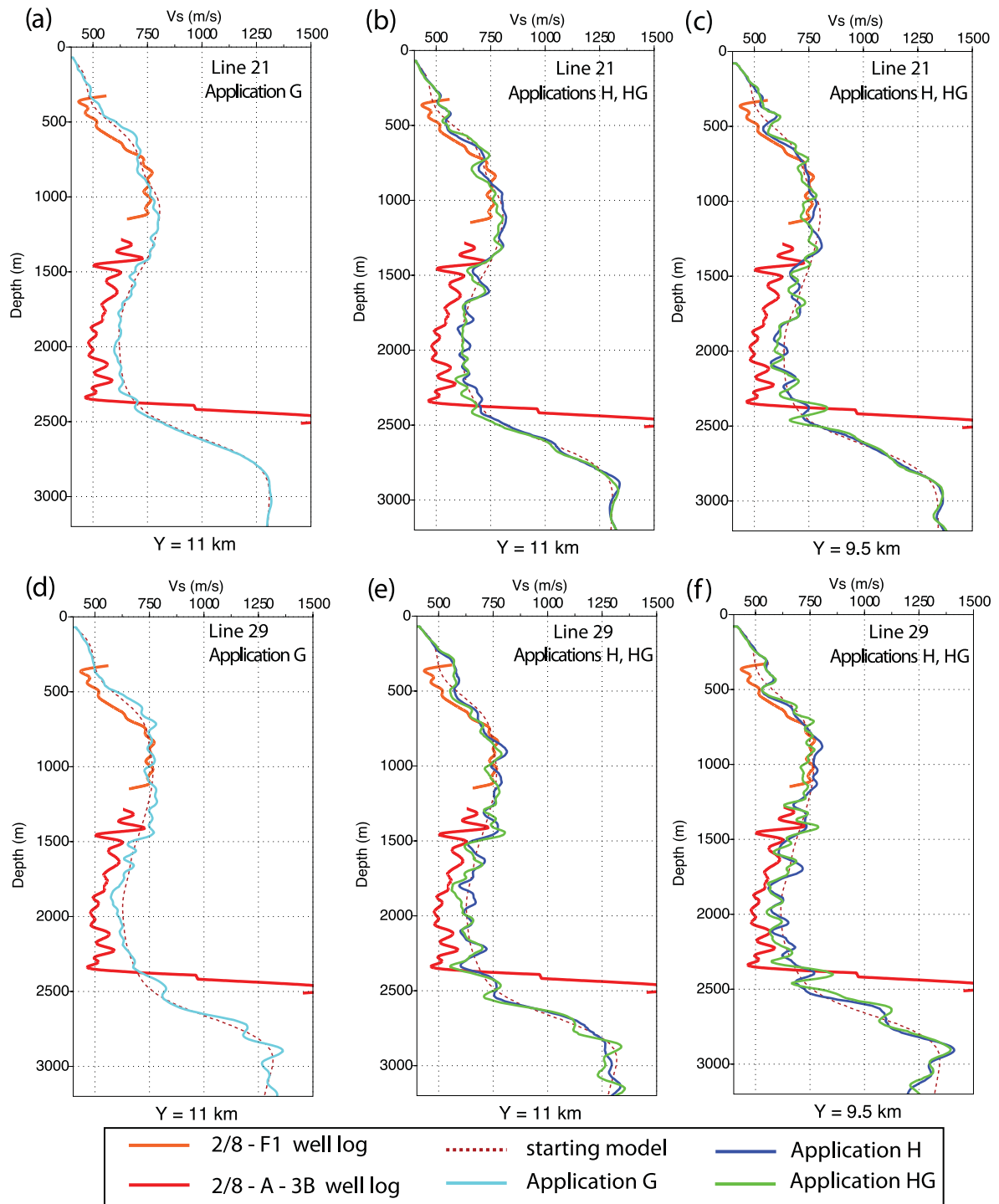
Figure 6. Comparison of two sonic logs (red and orange curves) and the profiles of the final *S*-wave velocity FWI model of line 21 (a–c) and line 29 (d–f). The FWI profile is extracted at the well log position (*Y* = 11 km), and also at *Y* = 9.5 km for the hierarchical strategy. The results obtained from application *G* (a,d), *H*, and *HG* (b, c, e, f) are in cyan, blue and green, respectively. The locations of the well logs are shown in fig. 14 of the Paper I.

recorded data. The direct comparison for the horizontal component of line 21 shows that the modelled amplitudes are even more underestimated.

The seismograms recorded by the horizontal geophones of line 21 clearly show the platform noise of the hyperbolic shape between −4 and −5 km in offset (Fig. 10a). The *PS*$_{2.6}$ arrival is not visible in the seismograms computed in the FWI models of application *HG* for the offset range corresponding to the platform location (Fig. 10b,

white lines), which thus suggests that the inversion is significantly hampered by this coherent noise. The noise does not only affect the imaging locally, but also everywhere in the medium. Indeed, the traces recorded by a receiver close to the platform are, whatever the offset, noisy, which hence affects the redundancy of the data sampling.

In Fig. 11, we show the behaviour of the misfit functions for applications *H*, *HG* and *G* from line 29. The misfit reduction for
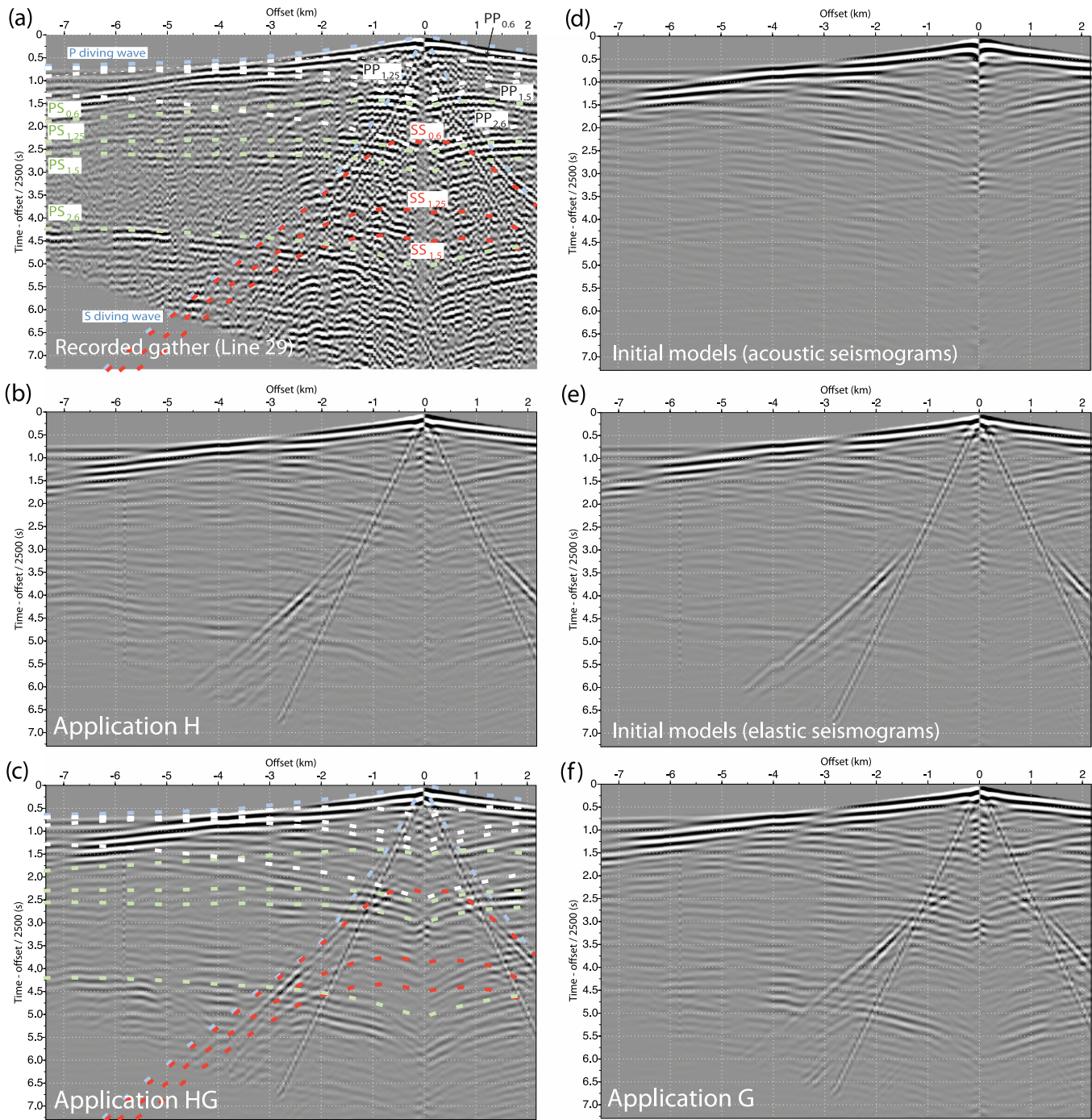
Figure 7. Shot gather recorded by the horizontal geophones of cable 29. The shot was located at $X_S = 12.5$ km. (a) Recorded data, on which traveltimes of the main converted waves are superimposed, as computed by ray tracing for the final FWI model of application *HG*. (b, c, f) Synthetic seismograms computed in the final FWI models of applications *H* (b), *HG* (c) and *G* (f). (d, e) Acoustic (d) and elastic (e) synthetic seismograms computed for the initial FWI models (see Fig. 3d, e) (the *S*-wave velocity model is not taken into account for acoustic modelling). PP$_i$, PS$_i$ and SS$_i$ denote *P–P*, *P–S* and *S–S* reflection, respectively (propagation in the water layer is not taken into account in the nomenclature), while the index i denotes the depth at which the reflection takes place.

application *H* is about 10 per cent, while it is less than 5 per cent for applications *HG* and *G*. It is shown in Paper I that the misfit reduction for the second step of our hierarchical approach (see Table 1) when inverting V_P, ρ and Q_P from the hydrophone, is about 15 per cent. We conclude that the misfit-function reduction decreases as the inversion progresses over the different hierarchical steps. This is however consistent with the overall strategy which consists of cancelling the data residuals associated with the dominant parameters first before

considering secondary effects associated with the influence of the shear wavespeed.

Source wavelet estimation

Another way to appraise the FWI models consists of estimating the source wavelet for each shot gather by solving a linear inverse problem, following the approach of Pratt (1999, eq. 17). The
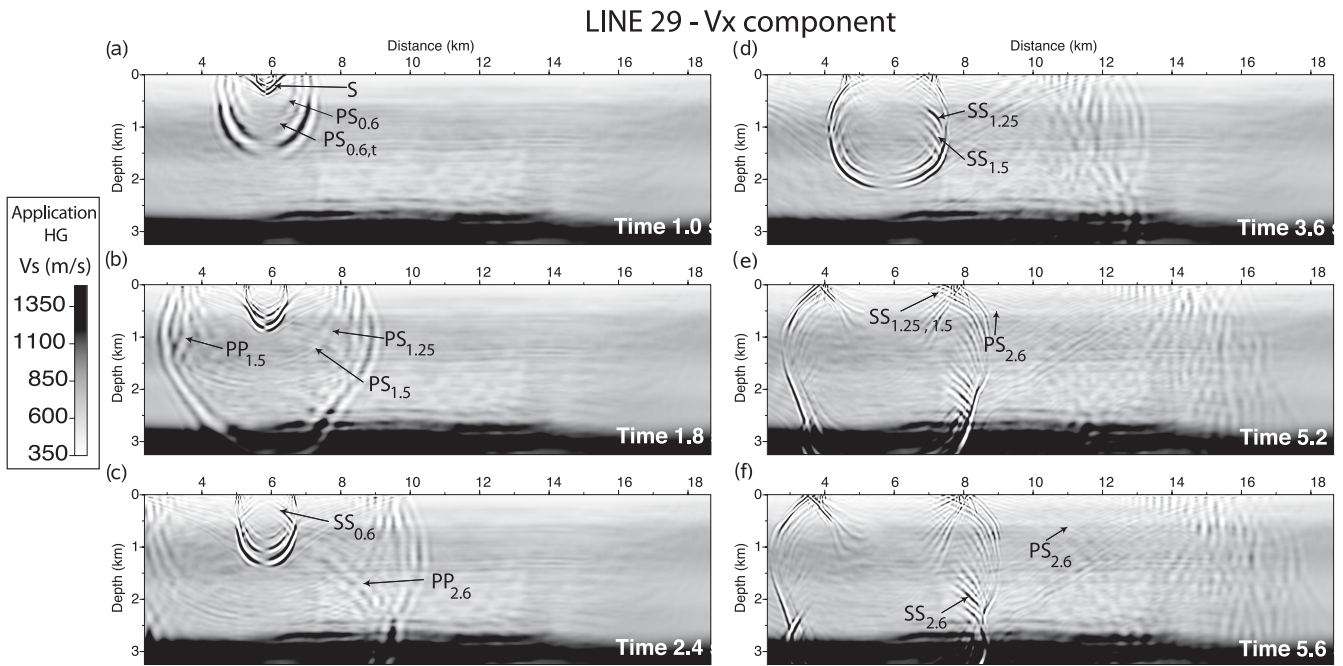
LINE 29 - Vx component

Figure 8. Snapshots of the elastic wavefields superimposed on the final *S*-wave velocity FWI model of application *HG*. See legend to Fig. 7 for nomenclature.
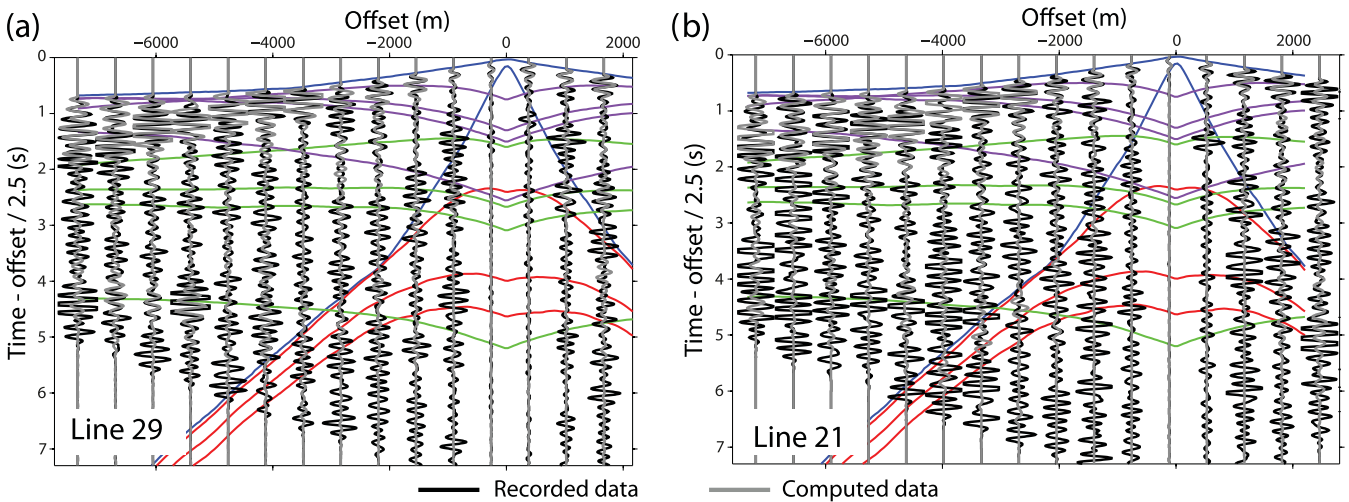

Figure 9. Direct comparison between recorded (black lines) and modelled (gray lines) seismograms of line 29 (a) and line 21 (b), for the horizontal geophone component. The synthetic seismograms are computed in the final FWI models of application *HG*.

repeatability of the source wavelet over the shots is an additional factor in favour of the relevance of the FWI models (Brenders & Pratt 2007; Jaiswal *et al.* 2009; Malinowski *et al.* 2011; Prieux *et al.* 2011). The peak-to-peak amplitude of the mean wavelet stacked over all of the shots can be used as the reference wavelet. The mean wavelet estimated per shot gather from each data component and from the initial and final FWI models (in all cases) is shown in Fig. 12 for line 29. Regardless of the component, we show progressive improvement of the peak-to-peak mean wavelet amplitude from the starting model to the final FWI models of applications *H* and *HG*. The mean wavelet amplitude inferred from the FWI model of application *HG* and from the hydrophone component is exactly the same as that inferred from the FWI model of application *H*, as the pressure is not inverted during application *HG*. We also note that the mean wavelets inferred from the FWI model of application

G always have smaller amplitude than those inferred from the FWI models of application *HG*. It can be shown that the mean wavelets inferred from the two geophone components are very similar, and that they differ from the wavelet inferred from the hydrophone. Remember that during the elastic inversion of the geophone data, the source is estimated from the two particle-velocity components.

In Fig. 13, we present the estimated wavelets that are computed for each shot, in the starting and final FWI models of application *HG* for the horizontal geophone components of lines 21 and 29. This shows relatively repeatable wavelets, except near the ends of the acquisition, where short offsets are lacking. The increase in the amplitude in the final model is mainly shown for the shots located near to the ends of the acquisition. The improvement in the wavelet focusing that is achieved in this study after elastic FWI is less significant than in the previous acoustic FWI applications
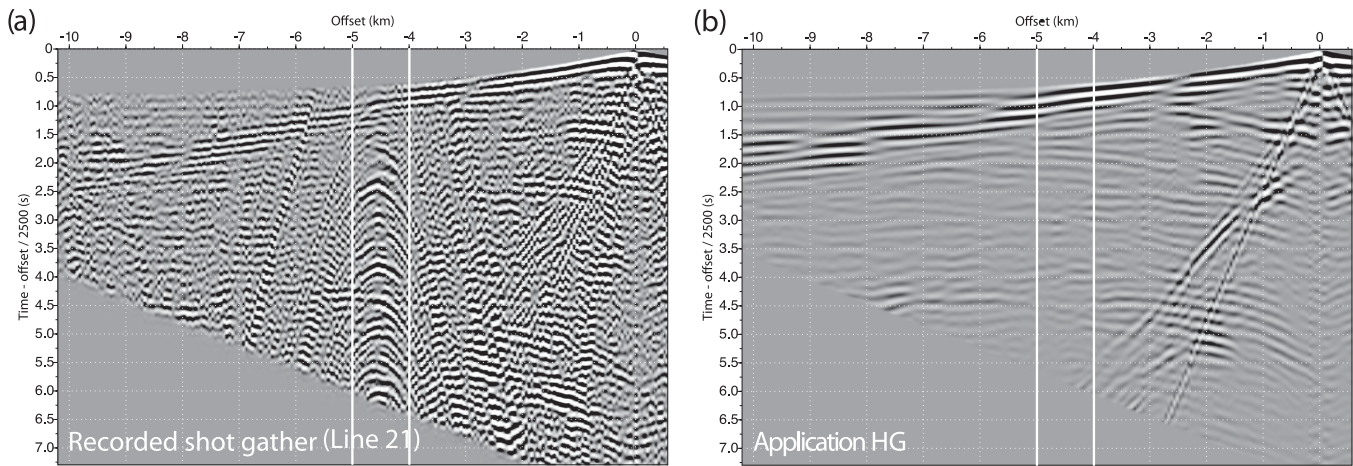
Figure 10. Shot gather recorded by the horizontal geophones of line 21. The shot was located at $X_S = 15.5$ km. (a) Recorded data. (b) Seismograms computed in the final FWI models of application *HG*. The offset range over which the platform noise pollutes the data is indicated by the white lines.
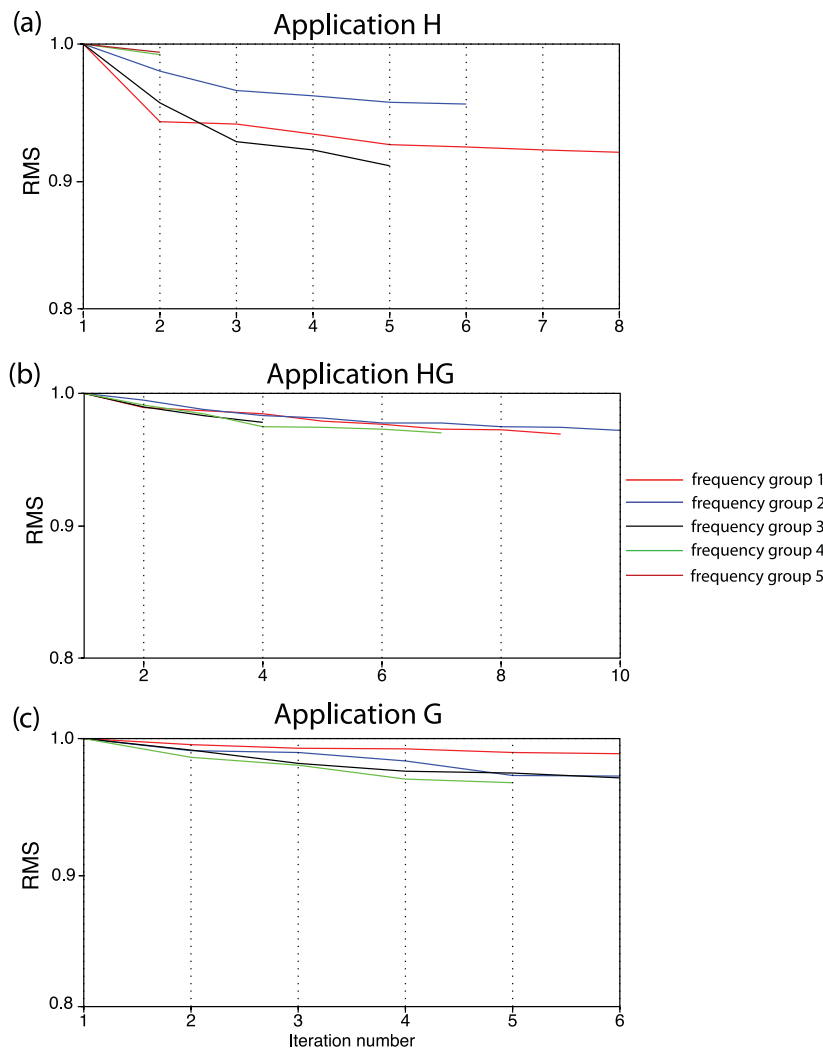

Figure 11. Normalized misfist function at different groups of frequencies for line 29, from the applications *H* (a), *HG* (b) and *G* (c).

(Malinowski *et al.* 2011; Prieux *et al.* 2011). The starting vertical *P*-wave velocity model that is used in this study for elastic FWI was built by visco-acoustic FWI during an earlier stage, and it accounts for a large part of the elastic wavefield. Therefore, the improvement in the wavelet focusing shown in this study mainly highlights the second-order contribution of the *S*-wave velocity structure to match the elastic wavefield. The footprint of the platform noise is also visible in the wavelet estimation along line 21 (Fig. 13b and d). There is some noise at the wavelet index of 175, which corresponds to an in-line position of 11.25 km, which is the platform location.
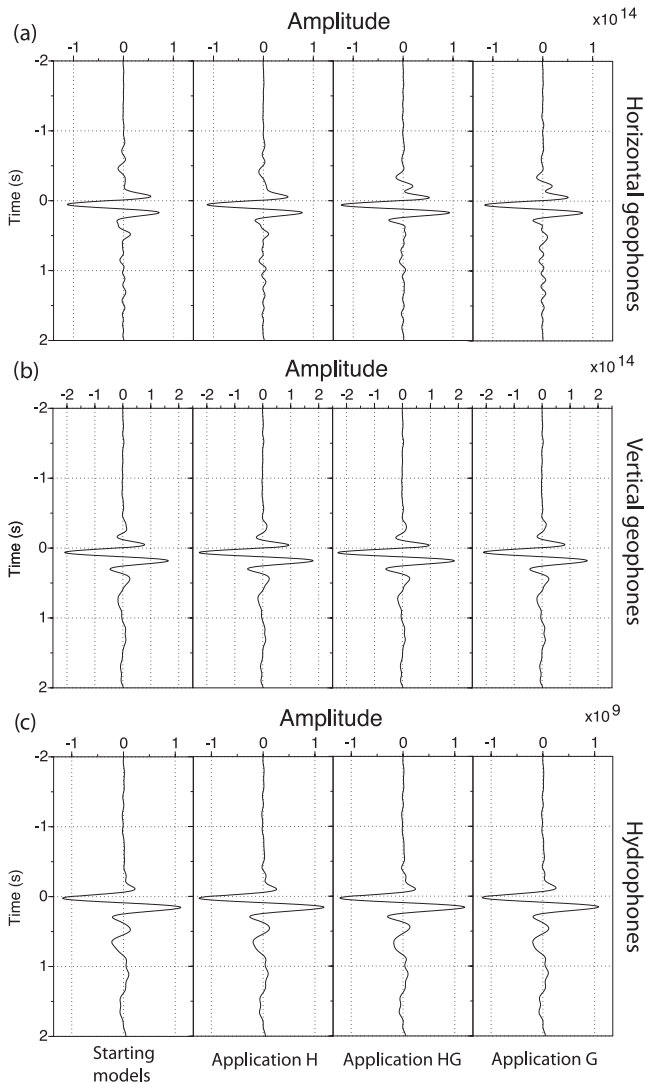
Figure 12. Mean estimated source wavelets computed for the starting models (first column) and for the final models of applications *H* (second column), *HG* (third column) and *G* (fourth column). (a–c) Wavelets estimated from the horizontal geophones (a), the vertical geophones (b) and the hydrophones (c) of line 29.

Geological implications

Poisson ratio and other combinations of V_P and V_S

We show a simplified geological scheme of the Valhall medium in Fig. 14 to help in the location of the different elements mentioned in the following. Interpretation of the vertical velocity, density and attenuation FWI models that were developed in Paper I suggests an accumulation of gas below barriers of claystones at 0.6 and 1.5 km in depth, and of soft quaternary sediments down to 0.6 km in depth. The elastic models developed in this study should help to confirm or deny this hypothesis, as the joint knowledge of the *P*-wave and *S*-wave velocities is known to be of interest for fluid characterization. Our level of confidence is however lowered because the elastic inversion did not recover the long spatial wavelengths of the V_S medium, and because it is difficult to interpret 2-D results in a zone where 3-D effects are expected, notably due to the gas zone.

In rock physics, the Poisson ratio is the ratio of the strain normal to and the strain parallel to a uni-axial stress applied to a unit cube of rock. The limiting values are 0 (for no auxetic materials), when the parallel strain is solely accounted for by a change in volume (no normal strain, such as for a cork), and 0.5 when the normal strain entirely balances the parallel strain (no volumetric change, such as for rubber and fluids). This quantity is thus related to compressibility, which increases as the Poisson ratio decreases. The presence of fluids in sediments tends to increase the compressibility, and hence this decreases the Poisson ratio. The Poisson ratio (ν) is expressed as a function of V_P and V_S as:

$$\nu = \frac{\frac{1}{2}\left(\frac{V_P}{V_S}\right)^2 - 1}{\left(\frac{V_P}{V_S}\right)^2 - 1}. \tag{7}$$

The *S*-wave velocity is less affected by the pore fluids than the *P*-wave velocity, as *S* waves only propagate in the solid matrix. The *P*-wave velocity decreases in gas-charged sediments, while the *S*-wave velocity does not change, hence decreasing the Poisson ratio. Fig. 15 shows some enlargements at different depths of the Poisson ratio models in the starting and final models of the application *HG* for line 21 and 29. In addition to the Poisson ratio, in Fig. 16, we show the ratio and the product between the *P* and *S* wavespeeds (denoted by V_P/V_S and $V_P \times V_S$ in the following). The V_P/V_S ratio allows areas saturated in fluids to be discriminated, and gives some insight into their physical state (in terms of pressure and temperature), while the $V_P \times V_S$ quantity is representative of the lithological variations and to the different porosities and/or crack densities, which minimizes at the same time the effects related to fluid saturation (Vanorio *et al.* 2005).

The $V_P \times V_S$ values derived from application *HG* of line 29 (Fig. 16b) are laterally continuous, and they show little variation down to a depth of 0.6 km, which supports the interpretation of soft unconsolidated quaternary sediments with a high homogeneous porosity. Below this depth, the sedimentary layers do not show significant lateral structural variations. In contrast, the V_P/V_S ratio in these layers (Fig. 16a) show more significant lateral variations, which can be interpreted as variations in the fluid content. We observe a significant decrease of the Poisson ratio at 0.6 km in depth in the models of application *HG*, at different locations for lines 21 and 29 (Figs 15a–d, black arrows), supporting our previous interpretation that gas (in the lower layer) accumulates below lithological barriers.

The elastic FWI generates the strongest perturbations at the reservoir level. The $V_P \times V_S$ map of line 29 (Fig. 16b) shows the stack of an upper layer between 2.6 and 2.8 km in depth, with a high $V_P \times V_S$ overlying a thin layer with a smaller $V_P \times V_S$. As $V_P \times V_S$ is sensitive to the porosity, we propose that the upper and lower layers correspond to the cap rock of the reservoir and the reservoir itself, respectively, where higher porosities are expected. This is consistent with the study of Barkved *et al.* (1999), who proposed that the strong porosity of the reservoir is responsible for the low value of the *P* impedance in the chalk, which can reach a value equal to, or even smaller than, that in tertiary sediments.

Some pinpoint areas with very low Poisson ratios are also shown below 2.7 km in depth (Fig. 15f). The interpretation of such detailed features at these depths probably goes beyond a reasonable level of confidence of the accuracy of our results. We nevertheless attempt to discuss their origin, as mainly a change in fluid saturation and/or in porosity, based on the Valhall literature. It is known that Valhall has a very high level of fluid saturation in the reservoir, which reaches up to 95 per cent (Munns 1985). This high saturation arises from the important porosity, which in some parts >50 per cent. On
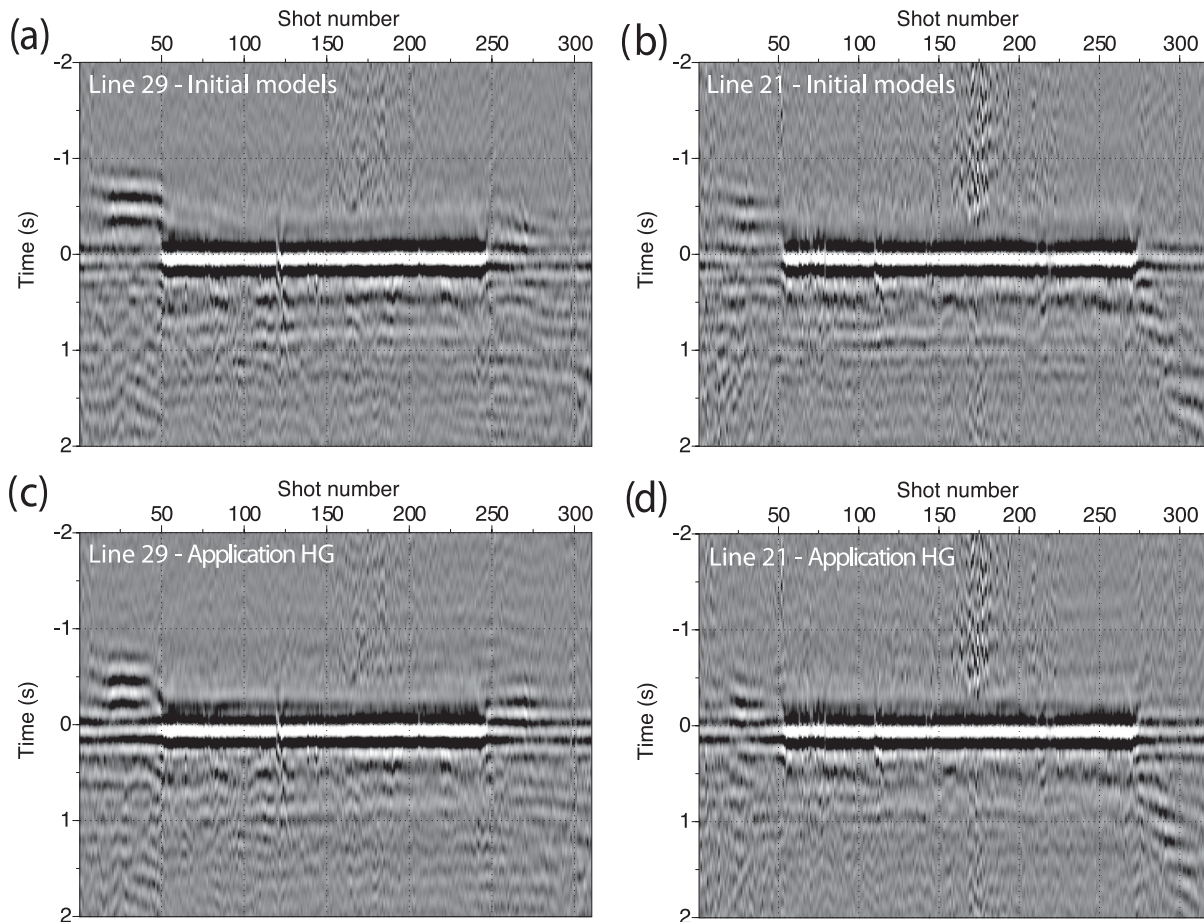
Figure 13. Source wavelets estimated for each shot gather for the starting models (a, b) and in the final FWI models (c, d) of application *HG*, from the horizontal geophones of line 29 (a, c) and line 21 (b, d). Note the footprint of the platform noise in (b, d) between the shot numbers of 150 and 200.
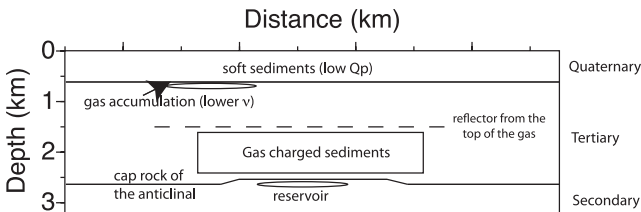

Figure 14. Geological structural scheme of the Valhall field.

the other hand, the reservoir area is known to be partitioned by faults that were created in the successive tectonic phases, and the porosity can vary significantly from one compartment to the next. Analysis of crossed dipole sonic logs in the chalk section by Mueller *et al.* (1997) showed that the *S* wavespeed is strongly affected by the porosity, with up to a 35 per cent reduction in velocity, as the porosity increases by 30 per cent. Vertical cracks and fractures are other possible causes of the Poisson ratio decrease, independent of the fluid saturation (Fortin *et al.* 2007). Azimuthal anisotropy is an indicator of porosity changes and fracturing. Mueller *et al.* (1997) showed from sonic logs that azimuthal anisotropy is of the order of 5 per cent to 10 per cent in magnitude in the upper chalk, where higher porosity is expected. Azimuthal anisotropy was also estimated from *S*-wave splitting by Olofsson *et al.* (2003) and was used for 4-D amplitude variation with offset and azimuth (AVOA) studies by Barkved *et al.* (2003). The V_P/V_S ratio showing more contrast in the reservoir than the $V_P \times V_S$ map may suggest that

fluid saturation is more significant than changes in porosity in the reservoir itself.

Hydrocarbon indicators

We now derive a popular hydrocarbon indicator known as the AVO product (AVO_P) (Castagna & Smith 1994). To produce this quantity, we need to define the *P* reflection coefficient R_P as:

$$R_P = \left(\frac{\Delta V_P}{V_P} + \frac{\Delta \rho}{\rho} \right) \Big/ 2, \tag{8}$$

where

$$
\begin{aligned}
V_P &= (V_{P,2} + V_{P,1})/2; & \Delta V_P &= V_{P,2} - V_{P,1}, \\
V_S &= (V_{S,2} + V_{S,1})/2; & \Delta V_S &= V_{S,2} - V_{S,1}, \\
\rho &= (\rho_2 + \rho_1)/2; & \Delta \rho &= \rho_2 - \rho_1.
\end{aligned} \tag{9}
$$

In eq. (9), the (1) and (2) denote the overlying and the underlying layers, respectively. Finally, the AVO_P is defined as:

$$AVO_P = R_P \left[-2 \left(\frac{V_S}{V_P} \right)^2 \frac{\Delta \rho}{\rho} + \frac{1}{2} \frac{\Delta V_P}{V_P} - 4 \left(\frac{V_S}{V_P} \right)^2 \frac{\Delta V_S}{V_S} \right]. \tag{10}$$

This formula allowed Djikpéssé & Tarantola (1999b) to clearly image the shale over a gas sand reservoir. In Fig. 17, we show this quantity computed for the starting models used for the acoustic and elastic FWI, and from the FWI models of application *HG* for lines
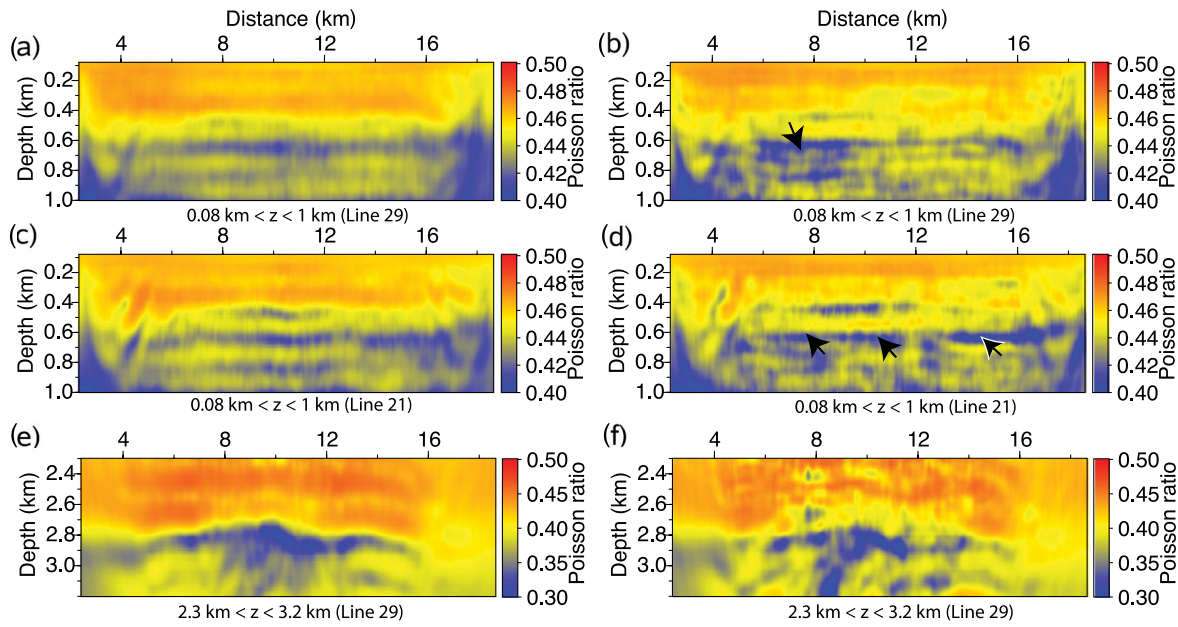
Figure 15. Poisson ratio models. Enlargements on the starting (left panels) and final (right panels) Poisson ratio models of application *HG* for lines 21 (c, d) and 29 (a, b, e, f, g, h), at different depths. Note that the colour scale changes across the panels. Black arrows, significative decrease in the Poisson ratio model associated with an accumulation of gas below lithological barriers.
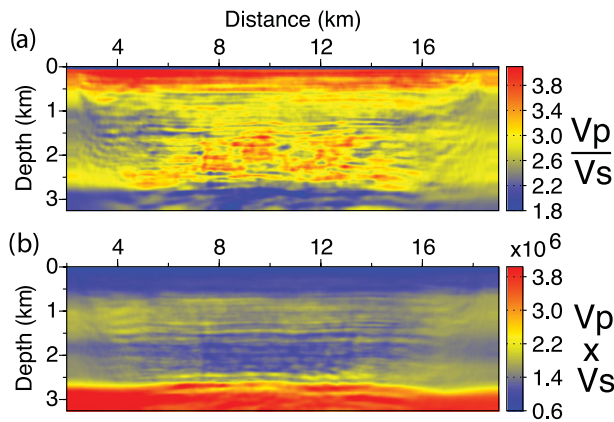

Figure 16. Ratio and product of *P*-wave velocity (V_P) and *S*-wave (V_S) velocity models. (a) V_P/V_S. (b) $V_P \times V_S$ (b) as inferred from the FWI models of application *HG* for line 29.

21 and 29. The AVO_P highlights in white the layers with hydrocarbon potential, like the reflectors below which there is an accumulation of gas at 0.6 and 1.5 km in depth. We also note that between 1.5 and 2.5 km in depth, the AVO_P map for line 21 shows some lower values than for line 29, which is consistent with a stronger gas content in the medium for line 21. The reservoir level logically shows the strongest negative values due to its high fluid content, although we note the acoustic starting model already had a white pattern in this area.

CONCLUSIONS

We have shown the feasibility of visco-elastic VTI FWI of multicomponent OBC data recorded in the Valhall oil field for the reconstruction of the vertical *P* wavespeed, the *S* wavespeed, the density and the quality factor. We have proposed a data-driven and parameter-driven FWI workflow adapted to this case study, which proceeds hierarchically over parameter classes and data compo-

nents, to reduce the nonlinearity of the multiparameter inversion. This hierarchical approach is justified by the limited influence on marine data sets of the *S* wavespeed compared to the *P*-wave velocity. A key feature of the FWI workflow is to update the intermediate wavelengths of the *S* wavespeed from the long-spread *P*–*P* reflections recorded on the hydrophone component, and to build an improved starting *S*-wave velocity model for a more resolving inversion of the geophone components. The visco-acoustic and visco-elastic multiparameter workflow that we present are not intended as an exhaustive study, as many hierarchical FWI strategies can be viewed, and due to its case dependency behaviour. Further studies on the anisotropic parametrization, together with the hierarchical strategies to adopt, are of primary importance for multiparameter inversion. This study was performed in two dimensions. It is likely that the increased data redundancy provided by the 3-D data set will facilitate the reconstruction of the *S* wavespeed in the marine environment. Therefore, the application of 3-D visco-elastic anisotropic FWI to wide-azimuth multicomponent data will be the aim of our future studies.
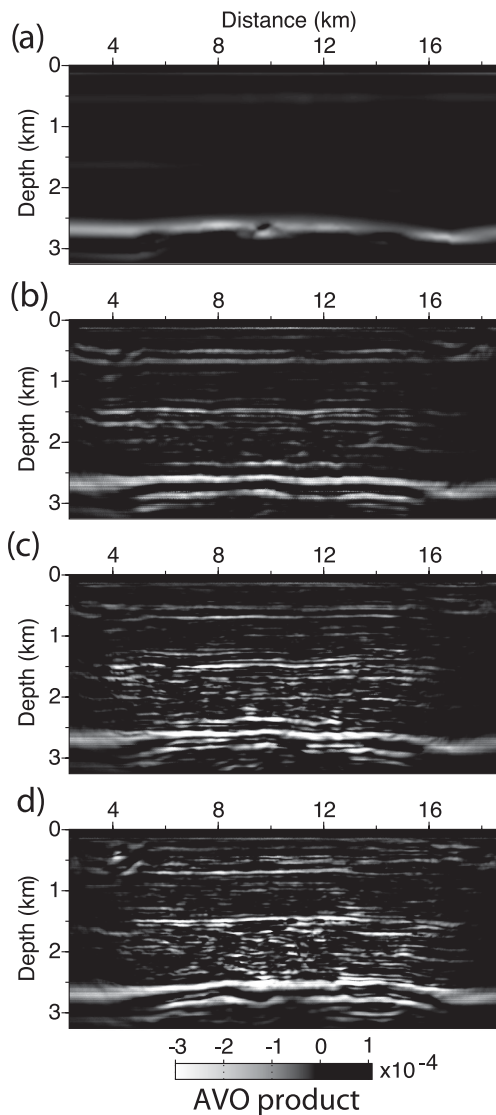
Figure 17. *AVO* product (see text for details). (a, b) The *AVO$_P$* computed in the initial acoustic (a) and elastic (b) models of line 29. The initial acoustic models are shown in Paper I. The initial elastic models are shown in Fig. 3. (c, d) The *AVO$_P$* computed in the final FWI models of application *HG* for line 29 (c) and 21 (d).

and we gratefully acknowledge both of these facilities and the support of their staff. We also thank BP Norge AS and their Valhall partner Hess Norge AS, for allowing access to the Valhall data set as well as to the well-log velocities.

REFERENCES

Aki, K. & Richards, P., 1980. *Quantitative Seismology: Theory and Methods,* W. H. Freeman & Co, New York.

Barkved, O., Mueller, M. & Thomsen, L., 1999. Vector interpretation of the valhall 3d/4c obs dataset, in *Proceedings of the 61th Annual EAGE Conference & Exhibition,* Helsinki, Finland, Extended Abstracts.

Barkved, O., Buer, K., Halleland, K., Kjelstadli, R., Kleppan, T. & Kristiansen, T., 2003. 4D seismic response or primary production and waste injection at the valhall field, in *Proceedings of the 65th Annual EAGE Conference & Exhibition,* Stavanger, Extended Abstracts.

Barnes, C. & Charara, M., 2009. The domain of applicability of acoustic full-waveform inversion for marine seismic data, *Geophysics,* **74,** WCC91–WCC103.

Baumstein, A., Ross, W. & Lee, S., 2011. Simultaneous source elastic inversion of surface waves, in *Proceedings of the 73rd EAGE Annual Conference and Exhibition,* Expanded Abstracts, C040, European Association of Geoscientists and Engineers.

Bleistein, N., 1986. Two and one half dimensional in plane wave propagation, *Geophys. Prospect.,* **34,** 686–703.

Brenders, A.J. & Pratt, R.G., 2007. Full waveform tomography for lithospheric imaging: results from a blind test in a realistic crustal model, *Geophys. J. Int.,* **168,** 133–151.

Brossier, R., Operto, S. & Virieux, J., 2009a. 2D elastic frequency-domain full-waveform inversion for imaging complex onshore structures, *Proceedings of the 71th Annual EAGE Conference & Exhibition,* Amsterdam, Expanded Abstracts, U019, European Association of Geoscientists and Engineers.

Brossier, R., Operto, S. & Virieux, J., 2009b. Seismic imaging of complex onshore structures by 2D elastic frequency-domain full-waveform inversion, *Geophysics,* **74,** WCC105–WCC118.

Brossier, R., Operto, S. & Virieux, J., 2009c. Two-dimensional seismic imaging of the Valhall model from synthetic OBC data by frequency-domain elastic full-waveform inversion, *SEG Tech. Prog. Expand. Abstr.,* **28,** 2293–2297.

Brossier, R., Gholami, Y., Virieux, J. & Operto, S., 2010a. 2D frequency-domain seismic wave modeling in VTI media based on a hp-adaptive discontinuous galerkin method, in *Proceedings of the 72nd Annual International Meeting,* Expanded Abstracts, C046, European Association of Geoscientists and Engineers.

Brossier, R., Operto, S. & Virieux, J., 2010b. Which data residual norm for robust elastic frequency-domain full waveform inversion? *Geophysics,* **75,** R37–R46.

Brossier, R., 2011. Two-dimensional frequency-domain visco-elastic full waveform inversion: parallel algorithms, optimization and performance, *Comput. Geosci.,* **37,** 444–455.

Bunks, C., Salek, F.M., Zaleski, S. & Chavent, G., 1995. Multiscale seismic waveform inversion, *Geophysics,* **60,** 1457–1473.

Castagna, J. & Smith, S., 1994. Comparison of avo indicators: a modeling study, *Geophysics,* **59,** 1849–1855.

Červený, V., Molotkov, I.A. & Pšenčik, I., 1977. *Ray Method in Seismology,* Charles University Press, Prague.

Chavent, G., 2009. *Nonlinear Least Squares for Inverse Problems,* Springer Dordrecht, Heidelberg, London, New York.

Crase, E., Pica, A., Noble, M., McDonald, J. & Tarantola, A., 1990. Robust elastic non-linear waveform inversion: application to real data, *Geophysics,* **55,** 527–538.

Crase, E., Wideman, C., Noble, M. & Tarantola, A., 1992. Nonlinear elastic inversion of land seismic reflection data, *J. geophys. Res.,* **97,** 4685–4705.

Debski, W. & Tarantola, A., 1995. Information on elastic parameters obtained from amplitude of reflected waves, *Geophysics,* **60,** 1426–1436.

Djikpéssé, H.A. & Tarantola, A., 1999a. Multiparameter l_1 norm waveform fitting: interpretation of gulf of mexico reflection seismograms, *Geophysics,* **64,** 1023–1035.

Djikpéssé, H.A. & Tarantola, A., 1999b. Multiparameter l_1 norm waveform fitting: interpretation of gulf of mexico reflection seismograms, *Geophysics,* **64,** 1023–1035.

Domenico, S.N., 1984. Rock lithology and porosity determination from shear and compressional wave velocity, *Geophysics,* **49,** 1188–1195.

Forgues, E. & Lambaré, G., 1997. Parameterization study for acoustic and elastic ray+born inversion, *J. Seism. Explor.,* **6,** 253–278.

Fortin, J., Guéguen, Y. & Schubnel, A., 2007. Effects of pore collapse and grain crushing on ultrasonic velocities and V_p/V_s, *J. geophys. Res.,* **112,** B08207, doi:10.1029/2005JB004005.

Freudenreich, Y., Singh, S. & Barton, P., 2001. Sub-basalt imaging using a full elastic wavefield inversion scheme, in *Proceedings of the 63th Annual EAGE Conference & Exhibition,* Amsterdam, Extended Abstracts, European Association of Geoscientists and Engineers.

Greenhalgh, S., Zhou, B. & Green, A., 2006. Solutions, algorithms and interrelations for local minimization search geophysical inversion, *J. Geophys. Eng.,* **3,** 101–113.

Gregory, A., 1976. Fluid saturation effects on dynamic elastic properties of sedimentary rocks, *Geophysics,* **41,** 895–921.

Hoven, J., Richardson, M. & Stoll, R., eds. 1991, *Assessment of shear strength of the sea bottom from shear wave velocity measurements on box cores and in-situ: shear waves in marine sediments,* Kluwer Academic Publishers, Dordrecht, the Netherlands.

Igel, H. & Schoenberg, M., 1995. Shear property estimation using marine pressure and additional ocean bottom recordings, in *Proceedings of the 57th Annual EAGE Conference & Exhibition,* Glasgow, UK, Extended Abstracts E040, European Association of Geoscientists and Engineers.

Igel, H., Djikpesse, H. & Tarantola, A., 1996. Waveform inversion of marine reflection seismograms for p impedance and poisson's ratio, *Geophys. J. Int.,* **124,** 363–371.

Jaiswal, P., Zelt, C., Dasgupta, R. & Nath, K., 2009. Seismic imaging of the Naga Thrust using multiscale waveform inversion, *Geophysics,* **74**(6), WCC129–WCC140.

Jannane, M. *et al.*, 1989. Wavelengths of Earth structures that can be resolved from seismic reflection data, *Geophysics,* **54,** 906–910.

Jin, S., Madariaga, R., Virieux, J. & Lambaré, G., 1992. Two-dimensional asymptotic iterative elastic inversion, *Geophys. J. Int.,* **108,** 575–588.

Lazaratos, S., Chikichev, I. & Wang, K., 2011. Improving the convergence rate of full wavefield inversion using spectral shaping, *SEG Tech. Prog. Expand. Abstr.,* 2011, 2428–2432.

Malinowski, M., Operto, S. & Ribodetti, A., 2011. High-resolution seismic attenuation imaging from wide-aperture onshore data by visco-acoustic frequency-domain full waveform inversion, *Geophys. J. Int.,* **186,** 1179–1204.

Manukyan, E., Latzel, S., Maurer, H., Marelli, S. & Greenhalgh, S., 2012. Exploitation of data-information content in elastic-waveform inversions, *Geophysics,* **77,** 105–115.

Miller, D., Oristaglio, M. & Beylkin, G., 1987. A new slant on seismic imaging: migration and integral geometry, *Geophysics,* **52,** 943–964.

Mueller, M., Barkved, O. & Thomsen, L., 1997. Dipole sonic results (Valhall area) - implications for AVO and OBS interpretation, in *Proceedings of the 59th Annual EAGE Conference & Exhibition,* Geneva, Switzerland, Extended Abstracts.

Munns, J.W., 1985. The Valhall field: a geological overview, *Mar. Pet. Geol.,* **2,** 23–43.

Muyzert, E., 2000. Scholte wave velocity inversion for a near surface S-velocity model and PS-statics. SEG Technical Program Expanded Abstracts, pp. 1197–1200.

Neves, F.A. & Singh, S.C., 1996. Sensitivity study of seismic reflection/refraction data, *Geophys. J. Int.,* **126,** 470–476.

Nocedal, J. & Wright, S.J., 1999. *Numerical Optimization,* Springer, New York, US.

Nocedal, J., 1980. Updating quasi-Newton matrices with limited storage, *Math. Comput.,* **35,** 773–782.

Olofsson, B., Probert, T., Kommedal, J. & Barkved, O., 2003. Azimuthal anisotropy from the Valhall 4C 3D survey, *Leading Edge,* **22,** 1228–1235.

Operto, S., Virieux, J., Dessa, J.X. & Pascal, G., 2006. Crustal imaging from multifold ocean bottom seismometers data by frequency-domain full-waveform tomography: application to the eastern Nankai trough, *J. geophys. Res.,* **111,** doi:10.1029/2005JB003835.

Plessix, R.E., 2006. A review of the adjoint-state method for computing the gradient of a functional with geophysical applications, *Geophys. J. Int.,* **167,** 495–503.

Pratt, R.G. & Worthington, M.H., 1990. Inverse theory applied to multi-source cross-hole tomography. Part I: acoustic wave-equation method, *Geophys. Prospect.,* **38,** 287–310.

Pratt, R.G., Shin, C. & Hicks, G.J., 1998. Gauss-Newton and full Newton methods in frequency-space seismic waveform inversion, *Geophys. J. Int.,* **133,** 341–362.

Pratt, R.G., 1999. Seismic waveform inversion in the frequency domain, part I: theory and verification in a physic scale model, *Geophysics,* **64,** 888–901.

Prieux, V., Brossier, R., Operto, S. & Virieux, J., 2013. Multiparameter full waveform inversion of multicomponent OBC data from Valhall. part 1: imaging compressional wavespeed, density and attenuation, *Geophys. J. Int.,* doi:10.1093/gji/ggt177.

Prieux, V., Brossier, R., Gholami, Y., Operto, S., Virieux, J., Barkved, O. & Kommedal, J., 2011. On the footprint of anisotropy on isotropic full waveform inversion: the Valhall case study, *Geophys. J. Int.,* **187,** 1495–1515.

Ravaut, C., Operto, S., Improta, L., Virieux, J., Herrero, A. & dell'Aversana, P., 2004. Multi-scale imaging of complex structures from multi-fold wide-aperture seismic data by frequency-domain full-wavefield inversions: application to a thrust belt, *Geophys. J. Int.,* **159,** 1032–1056.

Sears, T., Singh, S. & Barton, P., 2008. Elastic full waveform inversion of multi-component OBC seismic data, *Geophys. Prospect.,* **56,** 843–862.

Sears, T.J., Barton, P.J. & Singh, S.C., 2010. Elastic full waveform inversion of multicomponent ocean-bottom cable seismic data: application to alba field, U. K. North Sea, *Geophysics,* **75,** R109–R119.

Shi, Y., Zhao, W. & Cao, H., 2007. Nonlinear process control of wave-equation inversion and its application in the detection of gas, *Geophysics,* **72**(1), R9–R18.

Shipp, R.M. & Singh, S.C., 2002. Two-dimensional full wavefield inversion of wide-aperture marine seismic streamer data, *Geophys. J. Int.,* **151,** 325–344.

Sirgue, L. & Pratt, R.G., 2004. Efficient waveform inversion and imaging: a strategy for selecting temporal frequencies, *Geophysics,* **69,** 231–248.

Sirgue, L., Barkved, O.I., Dellinger, J., Etgen, J., Albertin, U. & Kommedal, J.H., 2010. Full waveform inversion: the next leap forward in imaging at Valhall, *First Break,* **28,** 65–70.

Sun, R. & McMechan, G., 1992. 2-D full wavefield inversion for wide-aperture, elastic, seismic data, *Geophys. J. Int.,* **111,** 1–10.

Tarantola, A., 1986. A strategy for non linear inversion of seismic reflection data, *Geophysics,* **51,** 1893–1903.

Tarantola, A., 2005. *Inverse Problem Theory and Methods for Model Parameter Estimation,* SIAM, Philadelphia, PA.

Tatham, R. & Stoffa, R., 1976. Vp/vs - a potential hydrocarbon indicator, *Geophysics,* **41,** 837–849.

Vanorio, T., Virieux, J., Capuano, P. & Russo, G., 2005. Three-dimensional seismic tomography from *P* wave and *S* wave microearthquake travel times and rock physics characterization of the Campi Flegrei Caldera, *J. geophys. Res.,* **110,** B03201, doi:10.1029/2004JB003102.

Virieux, J. & Operto, S., 2009. An overview of full waveform inversion in exploration geophysics, *Geophysics,* **74,** WCC1–WCC26.

Wang, Y. & Rao, Y., 2009. Reflection seismic waveform tomography, *J. geophys. Res.,* **114,** doi:10.1029/2008JB005916.

White, R.S. & Stephen, R.A., 1980. Compressional to shear wave conversion in oceanic crust, *Geophys. J. R. astr. Soc.,* **63,** 547–565.

Yedlin, M., Vorst, D.V. & Virieux, J., 2010. Uniform asymptotic conversion of Helmholtz data from 3D to 2D, *J. appl. Geophys.,* **78,** 2–8.